

# An Embedded Mesh Approach for Isogeometric Boundary Layers in Contact Mechanics

Eugenia Gabriela Loera Villeda <sup>a</sup>      Ivo Steinbrecher <sup>a\*</sup>      Alexander Popp<sup>a</sup>

<sup>a</sup>Institute for Mathematics and Computer-Based Simulation,  
University of the Bundeswehr Munich, Werner-Heisenberg-Weg 39, 85577, Neubiberg,  
Bavaria, Germany

---

## Abstract

This paper proposes a novel discretization workflow for contact problems in which the discretization of the contact interface is decoupled from that of the bulk domain. This separation enables independently tailored meshes for the contact interface and the bulk volume, allowing local requirements—such as element type and mesh resolution—to be addressed efficiently. Exploiting the boundary representation of CAD models, the contact interface of each body is discretized using a NURBS-based boundary layer mesh. This provides a smooth geometric description of the contact surface and enhanced inter-element continuity. The bulk domain is discretized using a structured Cartesian grid. To couple the resulting non-matching discretizations, an embedded mesh approach based on a mortar-type constraint formulation is employed. The paper describes in detail the proposed discretization workflow for generating both the isogeometric boundary layer and the structured Cartesian grid, and presents several strategies for constructing NURBS-based boundary layer meshes. Finally, a set of numerical examples is provided to validate the proposed approach.

*Keywords:* Embedded mesh method, Contact mechanics, Isogeometric Analysis, Mortar methods

---

## 1 Introduction

Contact problems are of fundamental importance, as they arise in a wide range of physical and biological systems. They are characterized by complex interface phenomena, including friction, wear, lubrication, and thermomechanical effects. Over the past decades, advances in numerical contact formulations, together with increasing computational resources, have enabled significant technological progress. Notable examples include improvements in vehicle safety through crash simulations and the assessment of wear-induced damage in machine components [1]. In the medical field, sophisticated contact models have been developed for the planning of maxillofacial surgery [2] and, more recently, for the development of endovascular treatment strategies for cerebral aneurysms [3], with an emphasis on incorporating patient-specific geometries.

In the following, we focus on contact formulations based on the finite element method (FEM), for which substantial research efforts have been devoted to improving accuracy and robustness. A central line of research concerns the development of contact discretizations for non-matching meshes, including node-to-segment (NTS) [4, 5, 6] and segment-to-segment (STS) [7, 8, 9] techniques. A particular class of STS approaches is formed by mortar formulations [10, 11, 12], which have gained increasing relevance in recent years, as they are especially well suited for finite deformation contact problems and finite sliding. Mortar methods enforce contact constraints in a weak sense and enable a variationally consistent treatment of non-penetration and frictional sliding conditions, thereby guaranteeing optimal convergence rates [13]. In [14], it was shown that, for unilateral contact, the maximum expected convergence order under uniform mesh refinement is  $O(h^{3/2})$  for shape functions of polynomial order  $p \geq 2$ . This result makes

---

\*Corresponding author:

Email addresses: [gabriela.loera@unibw.de](mailto:gabriela.loera@unibw.de) (Eugenia Gabriela Loera Villeda), [ivo.steinbrecher@unibw.de](mailto:ivo.steinbrecher@unibw.de) (Ivo Steinbrecher), [alexander.popp@unibw.de](mailto:alexander.popp@unibw.de) (Alexander Popp)

the use of higher-order interpolation questionable for contact problems unless combined with adaptive mesh refinement techniques. For a comprehensive overview of computational contact mechanics based on FEM, the reader is referred to the monograph by [13].

Classical finite element discretizations based on Lagrange polynomials exhibit significant drawbacks, as their  $C^0$  interelement continuity leads to a discontinuous normal vector field along the contact interface. This is particularly critical because, regardless of the chosen contact discretization technique, normal projections between the contacting bodies are required throughout the contact evaluation. A commonly adopted strategy to alleviate this issue is the construction of the normal field by averaging the normals of the surface elements surrounding a node. Nevertheless, numerical instabilities may arise, especially in problems involving large sliding, due to the non-smooth variation of contact variables as the slave node slides over the master interface [15, 16]. To mitigate these oscillations, geometric smoothing techniques based on Hermite, Bezier, spline, and NURBS basis functions have been proposed. The underlying idea is to employ higher-order interpolations on the contact interface to improve the accuracy of the contact tractions, while keeping the bulk discretization unchanged [17, 18, 19, 20, 21]. Although such approaches reduce these oscillations, they do not necessarily eliminate them entirely [16].

To address these drawbacks, contact formulations based on isogeometric analysis (IGA) have been developed, with many established FEM-based contact formulations adapted to the IGA framework. A comprehensive overview of computational contact formulations within IGA is provided in [15]. The central concept of IGA is the integration of computer-aided design (CAD) and engineering analysis by employing the same basis functions used in CAD for numerical simulations [22, 23]. In [24, 25], it was shown that IGA can deliver increased robustness and accuracy per degree of freedom compared to FEM, as it relies on B-spline-based basis functions such as non-uniform rational B-splines (NURBS) or T-splines. These basis functions possess particularly attractive properties for contact problems, as already emphasized in the first publication on IGA [22]: they enable an accurate and smooth representation of the contact interface and guarantee an interelement continuity of at least  $C^1$ , thereby yielding a continuous normal vector field. Nevertheless, while the higher-order continuity of NURBS offers clear advantages for contact algorithms, it may not be required throughout the bulk of the domain, as it does not necessarily improve spatial convergence rates and may instead lead to increased computational cost.

In comparison to finite element mesh generation, mesh generation in IGA is not as well established and can be particularly challenging, especially for complex geometries in three dimensions [26, 27]. Although the isogeometric boundary representation is provided by a CAD model, it lacks a true volumetric description and is therefore essentially “hollow”. To address this limitation, a volume parametrization conformal to the given boundary representation must be constructed, which can be a demanding task [28, 29, 30].

Building on the previous observations, we propose a novel discretization approach for contact problems. The approach is illustrated in Figure 1 for a two-dimensional contact configuration; however, it is applicable to both two- and three-dimensional contact problems. The procedure starts from the boundary representation (also referred to as B-rep) of the bodies involved in contact. For the two-dimensional setup depicted in Figure 1a, the B-rep is constructed using NURBS curves, whereas for three-dimensional configurations it is given by NURBS surfaces. In the proposed approach, the discretization of the contact interface is decoupled from that of the bulk domain. Starting from the isogeometric B-rep, a boundary layer mesh is generated by offsetting the NURBS B-rep inward into the body, exploiting the tensor-product structure of NURBS. The remaining bulk domain is subsequently discretized using a simple and easy-to-generate Cartesian mesh. The resulting discretization is shown in Figure 1b. In this configuration, a subset of the Cartesian mesh elements is intersected by the boundary layer mesh; these elements are referred to as *cut elements*.

The simplified mesh generation strategy underlying the proposed approach follows the idea of immersed boundary methods, in which a B-rep is embedded into a simple background mesh, thereby eliminating the need for a conforming volume parametrization. Immersed boundary methods (also referred to as non-boundary-fitted or fictitious domain methods) comprise a broad class of techniques, including the finite cell method [31], CutFEM [32], XFEM [33, 34], and embedded mesh methods [35]. These approaches have been successfully applied to a wide range of complex multiphysics problems, such as fluid–structure interaction (FSI) [36, 37], crack propagation [38], and, more recently, interfacial damage and debonding in composite materials [39]. A related discretization strategy was introduced in [40] under the name of the immersed boundary-conformal method (IBCM) for the solution of linear elliptic problems. Furthermore, in [41], this approach was employed for the analysis of linear elastic Kirchhoff–Love and Reissner–Mindlin shell structures to incorporate geometric features, such as holes, into shell models. To the authors’ knowledge, IBCM has not yet been extended to three-dimensional problems nor applied to unilateral contact problems.

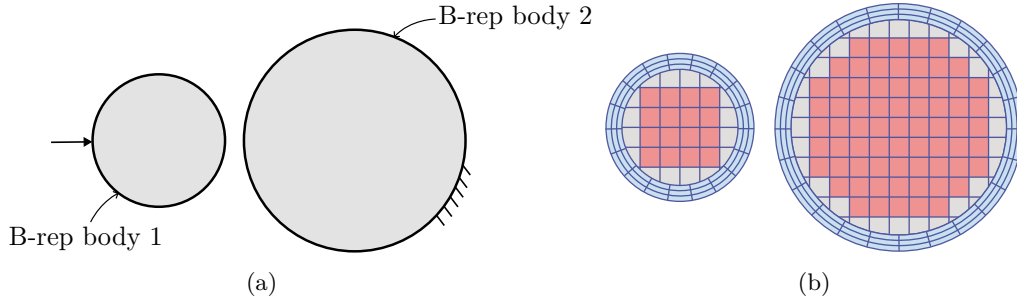


Figure 1: Two-dimensional contact problem between two bodies: (a) boundary conditions; (b) proposed discretization, in which each body is discretized with a NURBS boundary layer mesh (blue) and an underlying Cartesian mesh (red). Some elements of the Cartesian mesh, referred to as cut elements, are intersected by the boundary layer mesh (gray).

In this work, the boundary layer mesh is said to *overlap* the *underlying* Cartesian mesh, and the two discretizations are coupled by means of a mortar-based method. It is, however, well known that the application of mortar methods to embedded mesh discretizations may lead to an unstable Lagrange multiplier field and can induce locking effects [42]. To address this issue in the context of two-dimensional XFEM problems, the construction of so-called vital vertices was introduced in [43, 44] to ensure the stability of the Lagrange multiplier field. In the present work, special attention is given to the design of the discrete Lagrange multiplier space in order to avoid such instabilities for the problems considered here. With these considerations in mind, the applicability of the proposed approach to contact problems is demonstrated in Section 5.

The proposed approach leverages the advantages of IGA while simplifying mesh generation. First, the contact algorithm benefits from the high interelement continuity of isogeometric shape functions, which ensures a continuous normal vector field. Consequently, the drawbacks associated with  $C^0$ -continuous discretizations are naturally avoided. Furthermore, the boundary layer mesh and the bulk mesh can be tailored independently, allowing for local refinement in regions where contact is expected without affecting the Cartesian background mesh. Finally, the element technology can be selected independently for the boundary layer and the Cartesian meshes. Depending on the problem characteristics and the available software resources, one may choose a specific interpolation technology, such as an IGA-based discretization or classical Lagrangian shape functions, or employ more advanced element technologies to mitigate locking effects, including mixed or hybrid formulations [45] and enhanced assumed strain (EAS) elements [46].

The remainder of this paper is organized as follows. Section 2 presents the mesh generation workflow and investigates three approaches for constructing NURBS-based boundary layers. Section 3 introduces the governing equations of the contact problem and derives the embedded mesh formulation used to couple the isogeometric boundary layer with the Cartesian background mesh. Section 4 describes the spatial discretization and provides details on the numerical integration of cut elements. Section 5 presents several numerical examples to demonstrate the applicability of the proposed method to both two- and three-dimensional problems. Finally, Section 6 concludes the paper.

## 2 Mesh generation workflow

In this section, we describe the discretization approach adopted for the bodies involved in the contact problem shown in Figure 1b. The mesh generation workflow consists of two main steps. First, an isogeometric boundary layer mesh is constructed by performing an inward offset of the body's B-rep representation. Subsequently, a Cartesian mesh is generated to represent the bulk domain. In this work, three different methods for offsetting NURBS curves and surfaces are implemented and discussed. Finally, a simple algorithm for the construction of the Cartesian background mesh is presented.

### 2.1 NURBS geometries

This subsection briefly reviews the basic concepts of NURBS geometries relevant to this work. For a comprehensive discussion of this topic, the reader is referred to the monographs [47, 23]. Given a set of  $n$  B-spline basis functions of degree  $p$ , the  $i$ -th NURBS basis function is given by

$$R_i^p(\xi) = \frac{B_i^p(\xi)w_i}{\sum_{a=1}^n B_a^p(\xi)w_a}, \quad (1)$$

where  $B_i^p(\xi)$  denotes the  $i$ -th B-spline basis function and  $w_i$  its associated weight. In most engineering applications, these weights are positive.

Both NURBS and B-spline basis functions are defined over a non-decreasing sequence of parameter values, referred to as the knot vector. In the one-dimensional case, the knot vector is denoted by  $\Xi = \{\xi_1, \xi_2, \dots, \xi_{n+p+1}\}$  and is defined over the parametric domain  $\xi \in [\xi_1, \xi_{n+p+1}]$ . The individual entries  $\xi_i$  are called knots, and their multiplicity governs the continuity of the basis functions. In particular, a knot with multiplicity  $m_i$  yields  $C^{p-m_i}$  continuity at the corresponding parameter value  $\xi_i$ . An open knot vector is characterized by a multiplicity of  $p+1$  at the first and last knots, which results in interpolatory basis functions at the ends of the parameter interval  $[\xi_1, \xi_{n+p+1}]$ .

B-spline basis functions are constructed recursively using the Cox-de Boor formula [48, 49]. They possess several important properties: they form a partition of unity (i.e.,  $\sum_{i=1}^n B_i^p(\xi) = 1$ ), are non-negative and locally supported, and exhibit  $C^{p-1}$  continuity in the absence of repeated knots.

NURBS geometries are obtained as linear combinations of NURBS basis functions and control points. To this end, each control point  $\mathbf{P}_i$  is associated with a weight  $w_i$ . The set of  $n$  control points defining the geometry is referred to as the control polygon, denoted by  $\mathbf{P} = \{\mathbf{P}_1, \mathbf{P}_2, \dots, \mathbf{P}_n\}$ . For control points defined in a spatial dimension  $d$ , with  $\mathbf{P}_i \in \mathbb{R}^d$ , a NURBS curve is defined as

$$\mathbf{C}(\xi) = \sum_{i=1}^n R_i^p(\xi) \mathbf{P}_i. \quad (2)$$

Higher-dimensional geometries are constructed using tensor-product formulations. Let  $\mathbf{P}_{i,j} \in \mathbb{R}^d$  with indices  $i = 1, \dots, n$  and  $j = 1, \dots, m$ , polynomial orders  $p$  and  $q$ , and knot vectors  $\Xi = \{\xi_1, \dots, \xi_{n+p+1}\}$  and  $H = \{\eta_1, \dots, \eta_{m+q+1}\}$ . The resulting NURBS surface is expressed as

$$\mathbf{S}(\xi, \eta) = \sum_{i=1}^n \sum_{j=1}^m R_{i,j}^{p,q}(\xi, \eta) \mathbf{P}_{i,j}, \quad (3)$$

where the corresponding bivariate NURBS basis functions are given by

$$R_{i,j}^{p,q}(\xi, \eta) = \frac{B_i^p(\xi)B_j^q(\eta)w_{i,j}}{\sum_{a=1}^n \sum_{b=1}^m B_a^p(\xi)B_b^q(\eta)w_{a,b}}. \quad (4)$$

Analogously, a NURBS volume is constructed from control points  $\mathbf{P}_{i,j,k} \in \mathbb{R}^d$  with indices  $i = 1, \dots, n$ ,  $j = 1, \dots, m$ , and  $k = 1, \dots, l$ , polynomial orders  $p$ ,  $q$ , and  $r$ , and three knot vectors  $\Xi = \{\xi_1, \dots, \xi_{n+p+1}\}$ ,  $H = \{\eta_1, \dots, \eta_{m+q+1}\}$ , and  $Z = \{\zeta_1, \dots, \zeta_{l+r+1}\}$ . The resulting volume representation takes the form

$$\mathbf{V}(\xi, \eta, \zeta) = \sum_{i=1}^n \sum_{j=1}^m \sum_{k=1}^l R_{i,j,k}^{p,q,r}(\xi, \eta, \zeta) \mathbf{P}_{i,j,k}, \quad (5)$$

with the associated basis functions

$$R_{i,j,k}^{p,q,r}(\xi, \eta, \zeta) = \frac{B_i^p(\xi)B_j^q(\eta)B_k^r(\zeta)w_{i,j,k}}{\sum_{a=1}^n \sum_{b=1}^m \sum_{c=1}^l B_a^p(\xi)B_b^q(\eta)B_c^r(\zeta)w_{a,b,c}}. \quad (6)$$

NURBS geometries inherit the properties of their underlying basis functions. Owing to their local support, modifying a single control point influences at most  $p+1$  elements in its neighborhood. Furthermore, NURBS geometries satisfy a strong convex hull property, meaning that the geometry is entirely contained within the convex hull spanned by the control polygon.

## 2.2 Generation of an isogeometric boundary layer mesh

Within the IGA framework, mesh generation begins with the construction of the isogeometric B-rep representation of the body. Depending on the spatial dimension, this B-rep is described by a curve in two-dimensional settings or by a surface in three-dimensional problems. In the following, this initial representation is referred to as the *base B-rep*.

Table 1: Control points  $\mathbf{P}_i$  and weights  $w_i$  of a quadratic NURBS curve.

i	coordinates	$w_i$
1	(0.0, 0.0)	1.0
2	(0.2, 1.0)	$1/\sqrt{2}$
3	(1.0, 1.3)	1.0
4	(1.8, 0.8)	$1/\sqrt{2}$

The generation of an isogeometric boundary layer mesh exploits the tensor-product structure of NURBS surfaces and volumes. The basic idea is to extend the parametric representation of the base B-rep by a distance  $\ell$  along its inward normal direction. This is achieved by applying an offset operation, resulting in an *offset B-rep*. However, NURBS geometries cannot, in general, be offset analytically. This limitation can be illustrated for a NURBS curve  $\mathbf{C}(\xi)$ , whose offset curve  $\mathbf{C}_o$  is defined as

$$\mathbf{C}_o(\xi) = \mathbf{C}(\xi) + \ell \mathbf{n}(\xi), \quad (7)$$

where  $\mathbf{n}(\xi)$  denotes the inward-facing unit normal vector of  $\mathbf{C}(\xi)$ . For a planar curve, this normal vector is given by

$$\mathbf{n}(\xi) = \frac{(y'(\xi), -x'(\xi))}{\sqrt{x'(\xi)^2 + y'(\xi)^2}}, \quad (8)$$

with  $\mathbf{C}'(\xi) = \partial\mathbf{C}(\xi) / \partial\xi = (x'(\xi), y'(\xi))$ .

Although the regularity of  $\mathbf{C}(\xi)$  guarantees that  $\mathbf{n}(\xi)$  is well defined along the curve, the normalization in equation (8) introduces a square root in the denominator. As a consequence, the resulting offset curve is generally non-rational. Therefore, approximation techniques must be employed to compute offsets of NURBS geometries.

Extensive research has addressed the offsetting of rational curves, as this operation plays a central role in CAD/CAM, robotics, and numerous industrial applications, including NC machining [50, 51, 52]. However, many of the existing algorithms are not directly applicable in the present context, since the offset B-rep is required to preserve the parametric structure of the base B-rep, i.e., the polynomial degree and knot vectors must remain unchanged.

To this end, three approaches for offsetting the base B-rep while preserving its parametric representation are compared. The resulting offset B-rep defines the coupling interface  $\Gamma_*^{(i)}$  between the boundary layer mesh and the background mesh of body  $i$ , where the coupling conditions are imposed. It should be emphasized that the considered approximation techniques do not yield an exact offset of the base geometry, and a certain approximation error is therefore unavoidable. However, the interface  $\Gamma_*^{(i)}$  constitutes an artificial internal boundary separating the boundary layer and bulk discretization regions and does not carry any physical meaning; it merely serves as the domain on which the embedded mesh coupling conditions are enforced. Consequently, an exact geometric offset is not required for the construction of  $\Gamma_*^{(i)}$ .

In the following, only NURBS geometries represented by open knot vectors are considered. Although the extension of the presented approaches to NURBS surfaces is straightforward, the methodology is illustrated using a two-dimensional NURBS curve shown in Figure 2a. The curve has polynomial degree  $p = 2$  and is defined by the knot vector  $\Xi = \{0, 0, 0, 0.5, 1, 1, 1\}$  and a set of control points  $\mathbf{P}_i \in \mathbb{R}^2$  and weights  $w_i$ , with  $i = 1, \dots, 4$ . These values are listed in Table 1. To avoid self-intersecting offsets, the offset distance  $\ell$  is assumed to be smaller than the global minimum radius of curvature of the geometry. In all approaches, the offset control points  $\mathbf{P}_o$  inherit the same weights as their corresponding control points of the base B-rep.

1. Following the approach of [53], the first method operates directly on the control polygon of the base B-rep. For a NURBS curve, each line segment of the control polygon is translated by the offset distance  $\ell$  in the direction normal to the segment, as illustrated in Figure 2b. The new control points are then obtained from the intersections of the translated segments.

For NURBS surfaces, the method is extended by translating the control polygon, which is composed of planar facets. Each control point is determined as the intersection of its adjacent offset planes. Since a control point is connected to four planes, the intersection of any three adjacent planes is sufficient to uniquely determine its position; the specific choice of planes is arbitrary.

2. The second method is based on the approach presented in [54] and illustrated in Figure 2c. It determines the offset control points by interpolating a set of points  $\mathbf{x}_o = [\mathbf{x}_{o,1}, \mathbf{x}_{o,2}, \dots, \mathbf{x}_{o,n}]^\top$ . These points are obtained by evaluating the offset curve at the Greville abscissae  $\Xi_G = \{\xi_{G,1}, \xi_{G,2}, \dots, \xi_{G,n}\}$  [55], defined as

$$\xi_{G,i} = \frac{1}{p} \sum_{k=1}^p \xi_{i+k}, \quad i = 1, \dots, n. \quad (9)$$

The corresponding offset points are computed as

$$\mathbf{x}_{o,i} = \mathbf{C}(\xi_{G,i}) + \ell \mathbf{n}(\xi_{G,i}) \quad (10)$$

and subsequently interpolated using the same NURBS shape-function matrix  $\mathbf{N}$  employed for the base curve. The offset control points  $\mathbf{P}_o = [\mathbf{P}_1, \dots, \mathbf{P}_n]^\top$  are therefore obtained by solving

$$\mathbf{N}\mathbf{P}_o = \mathbf{x}_o. \quad (11)$$

3. The third method follows the approach proposed in [56], which involves solving an optimization problem to determine the position of the control points that best approximate the offset curve. The procedure begins by computing the exact offset position  $\mathbf{x}_{o,i}$  at a sampling point  $\xi_i$  along the base curve, as done in (10). The number of sampling points  $m$  is user defined. Next, a system of elastic springs is defined, where each spring connects an offset point  $\mathbf{x}_{o,i}$  to its corresponding base-curve point  $\mathbf{x}_i = \mathbf{C}(\xi_i)$ . The resulting spring system is shown in Figure 2d. For a  $m$  number of springs (with stiffness  $k = 1$ ), the total energy of the spring system is defined as

$$E(\mathbf{P}_o) = \frac{1}{2} \sum_{i=1}^m (u_i(\mathbf{P}_o))^2, \quad (12)$$

where the displacement of a spring  $u_i(\mathbf{P}_o)$  is defined as

$$u_i(\mathbf{P}_o) = \|\mathbf{x}_{o,i} - \mathbf{x}_i(\mathbf{P}_o)\|. \quad (13)$$

The energy of the spring system  $E(\mathbf{P}_o)$  serves as the objective function to be minimized using the gradient descent method. During the optimization process, the positions of the control points  $\mathbf{P}_o$  are iteratively updated to minimize the objective function, thereby yielding a curve that closely approximates the offset.

Figure 2 illustrates the offset curves obtained with the different approaches. All methods provide a qualitatively accurate approximation of the analytical offset. While such accuracy is sufficient for the intended application, we provide a quantitative comparison of the proposed approaches in the following to assess their interpolation quality compared to each other.

To this end, the pointwise distance between the approximated offset curve  $\mathbf{C}_{o,approx}(\xi)$  and the analytical offset is evaluated. At a parametric location  $\xi$ , the distance is defined as

$$d(\xi) = \|\mathbf{C}_{o,approx}(\xi) - (\mathbf{C}(\xi) + \ell \mathbf{n}(\xi))\|. \quad (14)$$

Local deviations are quantified by the maximum error  $e_\infty$ , computed from  $d(\xi)$  by densely sampling the parametric domain of  $\mathbf{C}_{o,approx}(\xi)$ . To assess the global approximation quality, a length-normalized  $L^2$ -type error measure is introduced,

$$e_{L^2} = \left( \frac{1}{s_o} \int_{\Gamma^*} d(\xi)^2 ds \right)^{1/2}, \quad (15)$$

where  $s_o$  denotes the arc-length of  $\mathbf{C}_{o,approx}(\xi)$ .

The error measures are evaluated for the results shown in Figure 2 and summarized in Table 2. For the considered example, the optimization-based approach exhibits the smallest local deviations, as measured by  $e_\infty$ , and achieves the highest global accuracy in terms of  $e_{L^2}$ . It is closely followed by the interpolation-based method, whereas the control-polygon translation approach yields larger deviations according to both metrics.

As previously mentioned, the offset approaches can be extended to NURBS surfaces. The performance of the methods is demonstrated using a NURBS surface B-rep with the following characteristics:

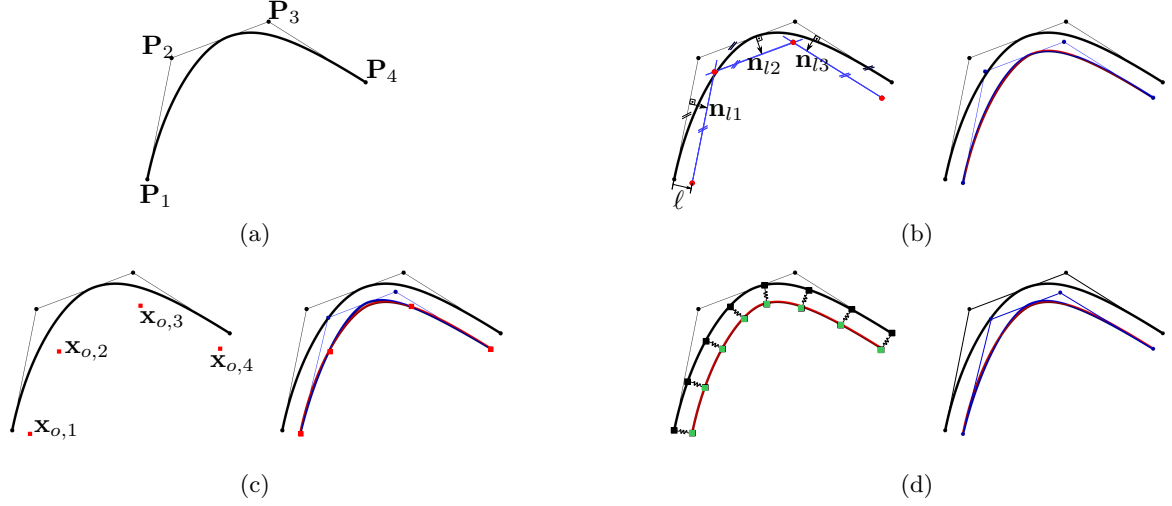


Figure 2: Implemented approaches for the offset of a B-rep. For all methods, the resulting offset (blue) is compared qualitatively with the analytical solution (red). (a) Quadratic NURBS base curve with knot vector  $\Xi = \{0, 0, 0, 0.5, 1, 1, 1\}$ . (b) Control-polygon translation, where intersections of the line segments are marked by  $\bullet$ . (c) Interpolation method with  $\Xi_G = \{0, 0.33, 0.66, 1\}$ . The sampling points  $\mathbf{x}_{o,i}$  are denoted by  $\blacksquare$ . (d) Optimization of a spring system: sampling points of the base curve  $\mathbf{x}_i$  and offset  $\mathbf{x}_{o,i}$  are denoted by  $\blacksquare$  and  $\blacksquare$ , respectively. Control points of the base  $\mathbf{P}_i$  and offset  $\mathbf{P}_{o,i}$  are indicated by  $\bullet$  and  $\bullet$ , respectively.

Table 2: Error measures for the considered offset methods applied to a NURBS curve.

Offset method	$e_\infty$	$e_{L^2}$
Control-polygon translation	3.599e-2	2.320e-2
Interpolation	2.646e-2	1.095e-2
Optimization	1.386e-2	9.724e-3

Table 3: Control points  $\mathbf{P}_{i,j}$  of a cubic NURBS surface.

$i$	$j$	coordinates	$i$	$j$	coordinates
1	1	(-25, -25, -10)	4	1	(-25, 5, 0)
1	2	(-15, -25, -8)	4	2	(-15, 5, -4)
1	3	(-5, -25, -5)	4	3	(-5, 5, -8)
1	4	(5, -25, -3)	4	4	(5, 5, -8)
1	5	(15, -25, -8)	4	5	(15, 5, -4)
1	6	(25, -25, -10)	4	6	(25, 5, 2)
2	1	(-25, -15, -5)	5	1	(-25, 15, -5)
2	2	(-15, -15, -4)	5	2	(-15, 15, -4)
2	3	(-5, -15, -3)	5	3	(-5, 15, -3)
2	4	(5, -15, -2)	5	4	(5, 15, -2)
2	5	(15, -15, -4)	5	5	(15, 15, -4)
2	6	(25, -15, -5)	5	6	(25, 15, -5)
3	1	(-25, -5, 0)	6	1	(-25, 25, -10)
3	2	(-15, -5, -4)	6	2	(-15, 25, -8)
3	3	(-5, -5, -8)	6	3	(-5, 25, -5)
3	4	(5, -5, -8)	6	4	(5, 25, -3)
3	5	(15, -5, -4)	6	5	(15, 25, -8)
3	6	(25, -5, 2)	6	6	(25, 25, -10)

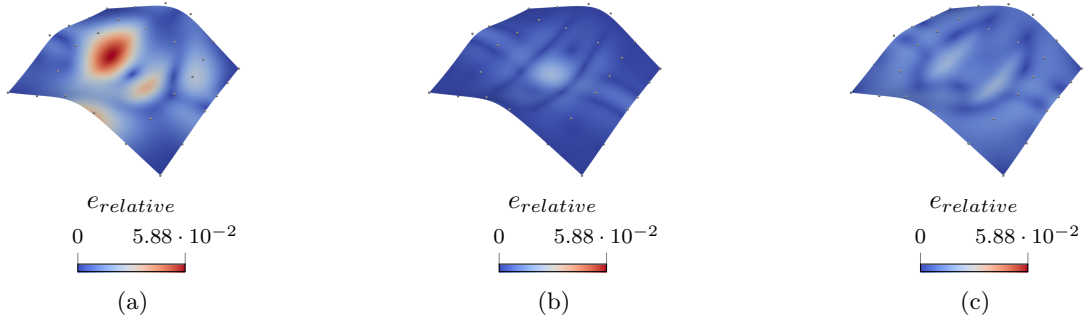


Figure 3: Relative error of the offset of a curved surface obtained by different offset methods: (a) control polygon translation, (b) interpolation method, (c) optimization of a spring system.

Table 4: Error measures for the considered offset methods applied to a NURBS surface.

Offset method	$e_\infty$	$e_{L^2}$
Control-polygon translation	7.403e-1	2.491e-1
Interpolation	2.082e-1	4.993e-2
Optimization	1.127e-1	6.225e-2

both parametric directions have polynomial degrees  $p = q = 3$ , and the corresponding knot vectors are  $\Xi = H = \{0.0, 0.0, 0.0, 0.0, \frac{1}{3}, \frac{2}{3}, 1.0, 1.0, 1.0, 1.0\}$ . The coordinates of the control points are listed in Table 3, and all control points have a weight of  $w_{i,j} = 1.0$ . The cubic NURBS B-rep is then offset using an offset thickness  $\ell = 3$ .

For this geometry, the relative error between the computed offset and the analytical solution is shown in Figure 3 for the different approaches. The largest deviations are observed for the control-polygon translation method, although the relative error remains below 6%. While both the interpolation and optimization approaches deliver similar overall accuracy, the optimization method exhibits wider regions with locally increased relative error compared to the interpolation method.

A more detailed assessment of the local and global accuracy is obtained by evaluating the maximum error  $e_\infty$  of the distance  $d(\xi, \eta)$  and an area-normalized  $L^2$ -type error, analogous to (15). The resulting values are summarized in Table 4. The optimization method yields the smallest local deviation, whereas the interpolation method achieves the smallest global error. The control-polygon translation method produces the largest deviations in both metrics.

More accurate offsets can be achieved by refining the base B-rep prior to applying the offset operation. In addition, for the optimization approach, the number and distribution of sampling points influence the quality of the offset, as discussed in [56]. However, a systematic investigation of these aspects is beyond the scope of the present work. For the intended application, the offset method is considered sufficient if the approximation error remains below a prescribed threshold and does not lead to distorted meshes.

In general, complex geometries cannot be represented by a single patch but instead require multiple patches. In the following, we consider geometries composed of multiple patches that are geometrically coincident and parametrically conforming at their interfaces, i.e., they share the same knot vectors, polynomial degrees, and number of control points. When adjacent patches lack  $C^1$  continuity, for instance at sharp corners, their boundary normals differ, which leads to mismatched boundaries after offsetting, as illustrated in Figure 4a for two adjacent patches. To address this issue, the normals along the common edge  $\mathbf{n}_{P_j}$  are averaged across all adjacent patches  $j$  during the offset operation. This ensures coincident offset boundaries, as shown in Figure 4b.

**Remark 2.1.** Non-smooth geometries, such as sharp corners and edges, are generally undesirable in surface-based contact formulations relying on mortar (or other STS) approaches. This is because the weak enforcement of the contact constraints leads to a surface-based weighting of the gap function, which may result in large penetrations at vertices and sharp edges. To address this issue, a robust and accurate mortar-based finite element framework that unifies vertex, edge, and surface contact was proposed in [57]. In that framework, three appropriate sets of Lagrange multipliers are defined for the different geometric entities (vertices, edges, and surfaces), together with a variationally consistent discretization. This methodology can, in principle, be extended to the non-smooth geometries arising in

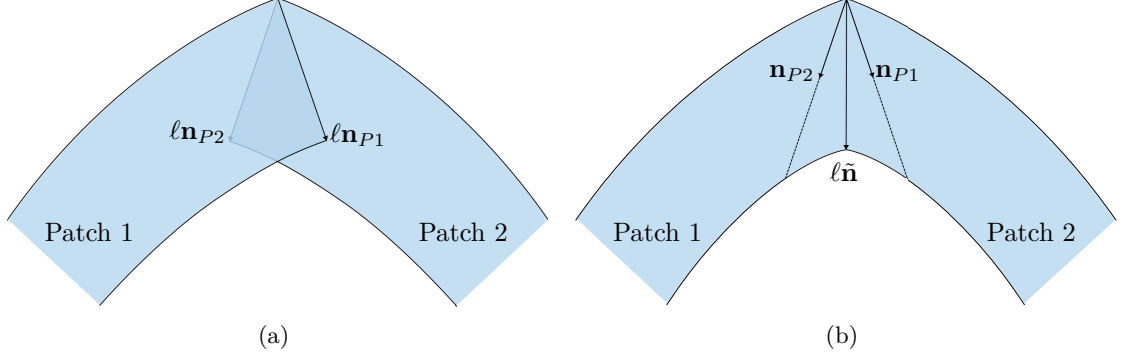


Figure 4: Coupling adjacent patches: (a) initial state after offsetting, (b) averaging of edges. First, the normal  $\mathbf{n}_{P_i}$  at each patch is evaluated at the edge and an average normal  $\tilde{\mathbf{n}}$  is evaluated.

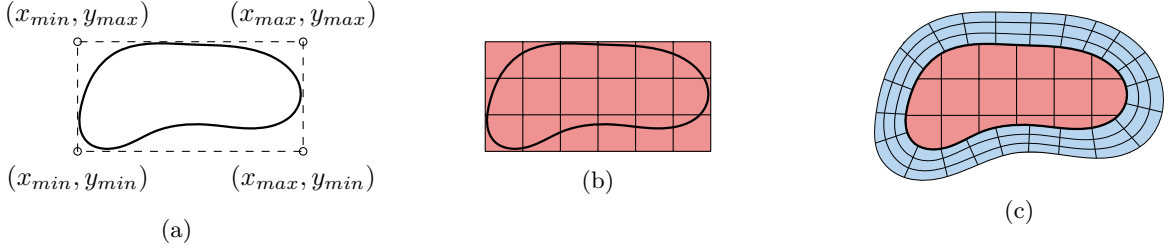


Figure 5: Generation of a Cartesian mesh: (a) definition of the AABB around  $\Gamma_*^{(i)}$ . (b) Discretization of an AABB using hexahedra-elements. (c) Complete discretization of the domain: boundary layer mesh and Cartesian mesh.

NURBS discretizations. However, a detailed discussion of such an extension lies beyond the scope of the present work.

### 2.3 Generation of a Cartesian mesh

After constructing the boundary layer mesh, the next step is the discretization of the bulk domain. For simplicity, a Cartesian mesh is employed. It is generated by defining an axis-aligned bounding box (AABB) around the interface  $\Gamma_*^{(i)}$ , as illustrated for a two-dimensional configuration in Figure 5a. The AABB is obtained by determining the minimum and maximum spatial coordinates of  $\Gamma_*^{(i)}$ , from which the bounding-box limits are defined. The resulting AABB is then discretized in a straightforward manner using either classical hexahedral elements or an isogeometric patch, as shown in Figure 5b. The complete discretization strategy, comprising the boundary layer mesh and the Cartesian background mesh, is illustrated in Figure 5c. As part of the coupling procedure, the Cartesian mesh is subsequently intersected by  $\Gamma_*^{(i)}$  through geometric cut operations. This procedure is discussed in more detail in Subsection 4.5.

## 3 Problem formulation

### 3.1 Contact problem statement

We consider a three-dimensional finite deformation contact problem involving two elastic bodies, as illustrated in Figure 6. The bodies  $i = 1, 2$  are represented by the open sets  $\Omega_0^{(i)} \subset \mathbb{R}^3$  in the reference configuration and by  $\Omega^{(i)}$  in the current configuration. For the sake of readability, and unless stated otherwise, all equations are assumed to hold for  $i = 1, 2$ . The finite deformation of each body is described by the deformation mapping  $\varphi^{(i)}$ .

The boundary  $\partial\Omega_0^{(i)}$  can be subdivided into the Dirichlet boundary  $\Gamma_u^{(i)}$ , the Neumann boundary  $\Gamma_\sigma^{(i)}$ , and the potential contact boundary  $\Gamma_c^{(i)}$ , on which displacements, tractions, and contact constraints are prescribed, respectively. These boundaries satisfy

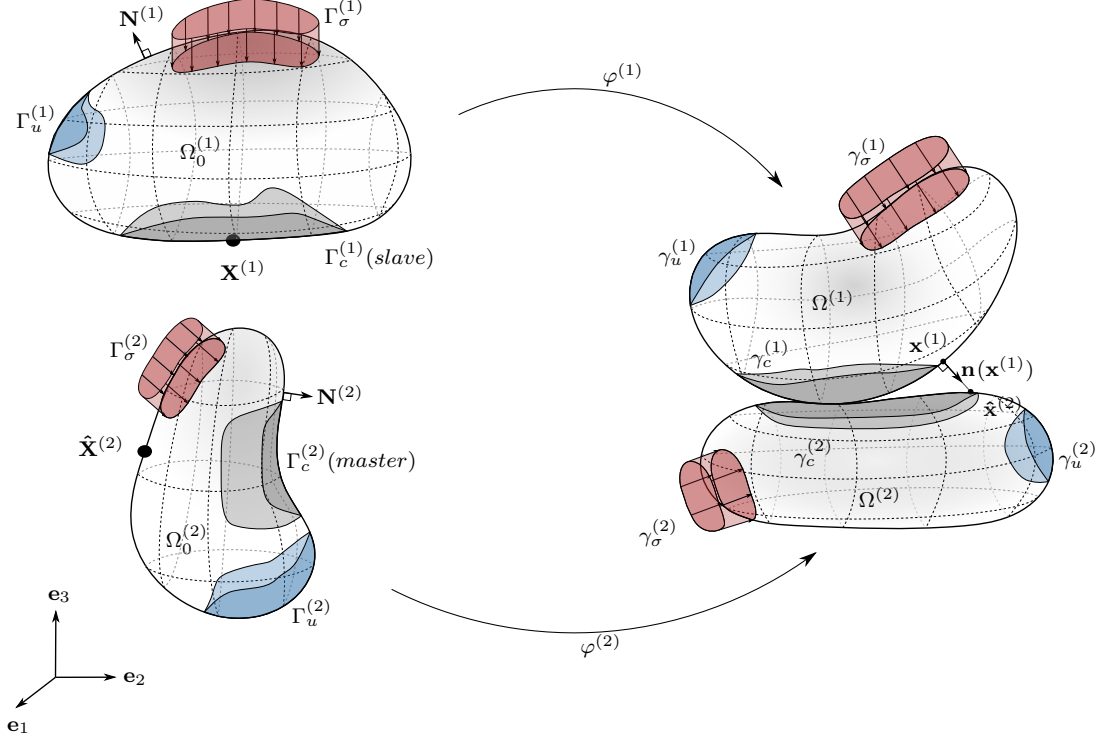


Figure 6: Setup of a three-dimensional contact problem.

$$\begin{aligned} \partial\Omega_0^{(i)} &= \Gamma_u^{(i)} \cup \Gamma_\sigma^{(i)} \cup \Gamma_c^{(i)}, \\ \Gamma_u^{(i)} \cap \Gamma_\sigma^{(i)} &= \Gamma_u^{(i)} \cap \Gamma_c^{(i)} = \Gamma_\sigma^{(i)} \cap \Gamma_c^{(i)} = \emptyset. \end{aligned} \quad (16)$$

In the current configuration, the corresponding boundaries are denoted by  $\gamma_u^{(i)}$ ,  $\gamma_\sigma^{(i)}$ , and  $\gamma_c^{(i)}$ , respectively. Following the standard nomenclature in contact mechanics,  $\Gamma_c^{(1)}$  is referred to as the *slave* surface, while  $\Gamma_c^{(2)}$  is referred to as the *master* surface. Let  $\mathbf{X}^{(i)}$  and  $\mathbf{x}^{(i)}$  denote the position of a material point in the reference and current configurations, respectively. The displacement field  $\mathbf{u}^{(i)}$  is then defined as

$$\mathbf{u}^{(i)} = \mathbf{x}^{(i)} - \mathbf{X}^{(i)}. \quad (17)$$

The strong form of the boundary value problem (BVP) of nonlinear elasticity reads

$$\begin{aligned} \nabla \cdot (\mathbf{F}^{(i)} \cdot \mathbf{S}^{(i)}) + \mathbf{b}_0^{(i)} &= \mathbf{0} && \text{in } \Omega_0^{(i)}, \\ \mathbf{u}^{(i)} &= \hat{\mathbf{u}}^{(i)} && \text{on } \Gamma_u^{(i)}, \\ \mathbf{P}^{(i)} \mathbf{N}^{(i)} &= \hat{\mathbf{t}}_0^{(i)} && \text{on } \Gamma_\sigma^{(i)}. \end{aligned} \quad (18)$$

Here,  $\mathbf{F}^{(i)}$  denotes the deformation gradient, while  $\mathbf{P}^{(i)}$  and  $\mathbf{S}^{(i)}$  represent the first and second Piola–Kirchhoff stress tensors, respectively. Furthermore,  $\mathbf{N}^{(i)}$  denotes the outward unit normal vector on  $\Gamma_\sigma^{(i)}$ , and the vector  $\mathbf{b}_0^{(i)}$  represents the body forces. The quantities  $\hat{\mathbf{u}}^{(i)}$  and  $\hat{\mathbf{t}}_0^{(i)}$  denote the prescribed displacement and traction, respectively. Without loss of generality, all formulations are presented for the quasi-static case. The extension to dynamic problems is straightforward.

Assuming homogeneous bodies with hyperelastic material behavior, the constitutive relation in the reference configuration is given by

$$\mathbf{S} = \frac{\partial \Psi}{\partial \mathbf{E}}, \quad (19)$$

where  $\Psi$  is the strain energy density function and  $\mathbf{E}$  denotes the Green–Lagrange strain tensor. In the numerical examples, the St. Venant–Kirchhoff material model is employed, with

$$\Psi_{\text{SVK}} = \frac{\lambda}{2}(\text{tr}\mathbf{E})^2 + \mu\mathbf{E} : \mathbf{E}, \quad (20)$$

where  $\lambda$  and  $\mu$  are the Lamé parameters [58].

For the solution of the contact problem, the gap function  $g_n(\mathbf{X}, t)$  is introduced to describe the non-penetration condition [59]. It is defined as

$$g_n(\mathbf{X}, t) = -\mathbf{n} \cdot [\mathbf{x}^{(1)}(\mathbf{X}^{(1)}, t) - \hat{\mathbf{x}}^{(2)}(\hat{\mathbf{X}}^{(2)}(\mathbf{X}^{(1)}, t), t)], \quad (21)$$

where  $\mathbf{n}$  denotes the outward unit normal vector at  $\mathbf{x}^1 \in \gamma_c^{(1)}$  in the current configuration. The point  $\hat{\mathbf{x}}^{(2)}$  is obtained from the closest-point projection of  $\mathbf{x}^1$  onto  $\gamma_c^{(2)}$ . The contact traction  $\mathbf{t}_c^{(1)}$  acting on the slave surface is decomposed into a normal component  $\mathbf{t}_n$  and a tangential component  $\mathbf{t}_\tau$ , such that

$$\mathbf{t}_c^{(1)} = \mathbf{t}_n + \mathbf{t}_\tau. \quad (22)$$

The normal component is given by  $\mathbf{t}_n = p_n \mathbf{n}$ , where  $p_n$  denotes the normal contact pressure. Although the proposed method can be extended to frictional contact, we consider frictionless sliding for simplicity, i.e.,  $\mathbf{t}_\tau = \mathbf{0}$ . The contact conditions are expressed by the Karush–Kuhn–Tucker (KKT) conditions,

$$g_n \geq 0, \quad p_n \leq 0, \quad g_n p_n = 0 \quad \text{on } \gamma_c^{(1)}. \quad (23)$$

Equations (18) and (23) constitute the strong form of the unilateral frictionless contact problem. To derive the weak formulation of (18), we introduce the solution space  $\mathcal{U}^{(i)}$  and the test space  $\mathcal{V}^{(i)}$  for the displacement field,

$$\mathcal{U}^{(i)} = \{\mathbf{u}^{(i)} \in H^1(\Omega_0^{(i)}) \mid \mathbf{u}^{(i)} = \hat{\mathbf{u}}^{(i)} \text{ on } \Gamma_u^{(i)}\}, \quad (24)$$

and

$$\mathcal{V}^{(i)} = \{\delta\mathbf{u}^{(i)} \in H^1(\Omega_0^{(i)}) \mid \delta\mathbf{u}^{(i)} = \mathbf{0} \text{ on } \Gamma_u^{(i)}\}, \quad (25)$$

where  $H^1(\Omega_0^{(i)})$  represents a Sobolev function space [60]. To enforce the contact constraints given in (23), a Lagrange multiplier field  $\boldsymbol{\lambda}$  is introduced, belonging to the space  $\mathcal{M}$  [12, 61]. This Lagrange multiplier can be interpreted as the contact traction, i.e.,  $\boldsymbol{\lambda} = -\mathbf{t}_c^{(1)}$ . The solution space  $\mathcal{M}$  is defined as the dual space of the trace space  $\mathcal{W}^{(1)}$  associated with  $\mathcal{V}^{(1)}$ , restricted to  $\gamma_c^{(1)}$ . For frictionless contact, a simplification can be done in the solution space  $\mathcal{M}$ . This simplification results in a convex cone of Lagrange multipliers defined as

$$\mathcal{M}^+ := \left\{ \boldsymbol{\mu} \in \mathcal{M} \mid \boldsymbol{\mu}_\tau = \mathbf{0}, \langle \boldsymbol{\mu}_n, w \rangle_{\gamma_c^{(1)}} \geq 0, w \in \mathcal{W}^+ \right\}, \quad (26)$$

where  $\langle \cdot, \cdot \rangle_{\gamma_c^{(1)}}$  denotes the duality pairing between the scalar components of the spaces  $\mathcal{M}$  and  $\mathcal{W}$  [62, 63]. Furthermore,  $\mathcal{W}^+$  is the closed, non-empty convex cone defined by  $\mathcal{W}^+ := \{w \in \mathcal{W} \mid w \geq 0\}$ .

With these definitions, the weak formulation of the frictionless contact problem reads: Find  $\mathbf{u}^{(i)} \in \mathcal{U}^{(i)}$  and  $\boldsymbol{\lambda} \in \mathcal{M}^+$  such that

$$-\delta\mathcal{W}_{\text{int,ext}}(\mathbf{u}^{(i)}, \delta\mathbf{u}^{(i)}) - \delta\mathcal{W}_{\text{co}}(\boldsymbol{\lambda}, \delta\mathbf{u}^{(i)}) = 0 \quad \forall \delta\mathbf{u}^{(i)} \in \mathcal{V}^{(i)}, \quad (27)$$

$$\delta\mathcal{W}_\lambda(\mathbf{u}^{(i)}, \delta\boldsymbol{\lambda}) \geq 0 \quad \forall \delta\boldsymbol{\lambda} \in \mathcal{M}^+. \quad (28)$$

The internal and external virtual work contribution  $\delta\mathcal{W}_{\text{int,ext}}$ , the contact contribution  $\delta\mathcal{W}_{\text{co}}$ , and the weak constraint contribution  $\delta\mathcal{W}_\lambda$  are given by [63]

$$-\delta\mathcal{W}_{\text{int,ext}} = \sum_{i=1}^2 \left[ \int_{\Omega_0^{(i)}} \mathbf{S}^{(i)} : \delta\mathbf{E}^{(i)} dV_0 - \int_{\Omega_0^{(i)}} \mathbf{b}_0^{(i)} \cdot \delta\mathbf{u}^{(i)} dV_0 - \int_{\Gamma_\sigma^{(i)}} \hat{\mathbf{t}}_0^{(i)} \cdot \delta\mathbf{u}^{(i)} dA_0 \right], \quad (29)$$

$$-\delta\mathcal{W}_{\text{co}} = \int_{\gamma_c^{(1)}} \boldsymbol{\lambda} \cdot (\delta\mathbf{u}^{(1)} - \delta\mathbf{u}^{(2)} \circ \chi) dA, \quad (30)$$

$$\delta\mathcal{W}_\lambda = \int_{\gamma_c^{(1)}} (\delta\lambda_n - \lambda_n) g_n dA. \quad (31)$$

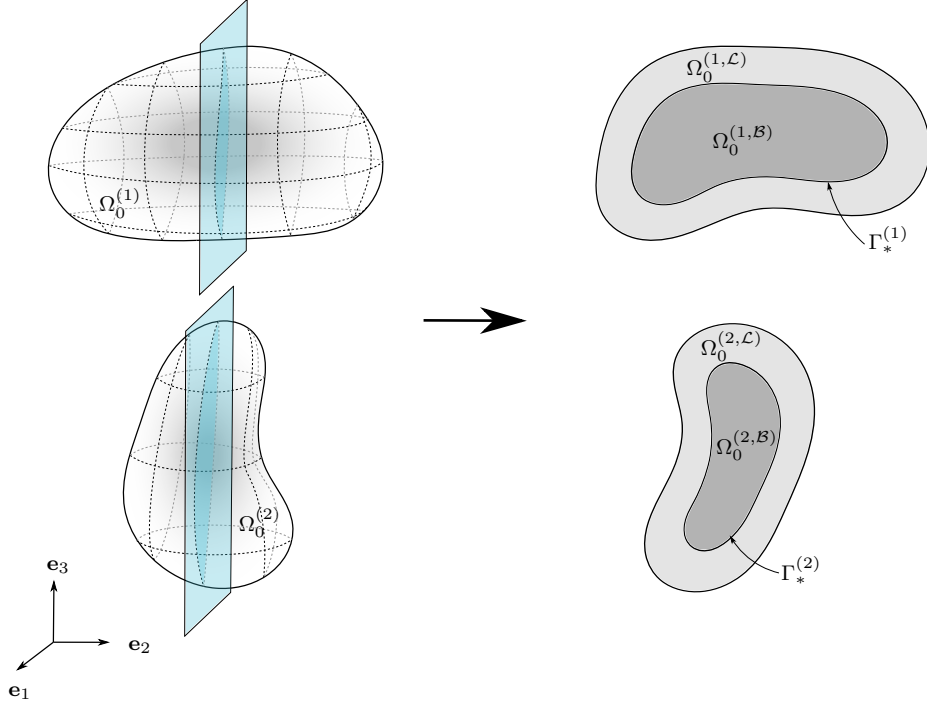


Figure 7: Subdivision of the solid domain into a boundary layer domain  $\Omega_0^{(i,\mathcal{L})}$  and a bulk domain  $\Omega_0^{(i,\mathcal{B})}$ , separated by the interface  $\Gamma_*^{(i)}$ . For the three-dimensional case, the subdivision is illustrated using a cross-section defined by the blue plane.

Here,  $\chi : \gamma_c^{(1)} \rightarrow \gamma_c^{(2)}$  denotes a suitable projection mapping from a point on the slave side to its corresponding point on the master side. For frictionless contact, it is sufficient to enforce the non-penetration condition in the normal direction only. Accordingly, in equation (31), the constraint is imposed using the scalar normal component  $\lambda_n$  of the Lagrange multiplier field.

### 3.2 Embedded mesh problem statement

So far, each solid body has been treated as a single domain. In the proposed approach, however, each contact body is subdivided into two subdomains: a boundary layer domain  $\Omega_0^{(i,\mathcal{L})}$  and a bulk domain  $\Omega_0^{(i,\mathcal{B})}$ . Furthermore, the interface  $\Gamma_*^{(i)}$  separates the two subdomains. This subdivision is illustrated in Figure 7 for the three-dimensional case. The body surface (and thus the contact boundary)  $\partial\Omega_0^{(i)}$ , as well as a portion of the adjacent volume, is contained in the boundary layer domain  $\Omega_0^{(i,\mathcal{L})}$ , whereas the bulk domain  $\Omega_0^{(i,\mathcal{B})}$  contains the remaining part of the body volume. Accordingly, the reference configuration satisfies

$$\Omega_0^{(i)} = \Omega_0^{(i,\mathcal{L})} \cup \Omega_0^{(i,\mathcal{B})}, \quad \Omega_0^{(i,\mathcal{L})} \cap \Omega_0^{(i,\mathcal{B})} = \emptyset. \quad (32)$$

In this work, homogeneous material properties are assumed. Consequently, both subdomains inherit the same material parameters as the original domain  $\Omega_0^{(i)}$ .

To couple the two subdomains, a coupling constraint is defined at the interface  $\Gamma_*^{(i)}$  and reads

$$\mathbf{u}^{(i,\mathcal{L})} - \mathbf{u}^{(i,\mathcal{B})} = \mathbf{0} \quad \text{on} \quad \Gamma_*^{(i)}. \quad (33)$$

As the proposed discretization approach described in Section 2 leads to overlapping meshes of  $\Omega_0^{(i,\mathcal{L})}$  and  $\Omega_0^{(i,\mathcal{B})}$ , a coupling constraint must be imposed between the two discretizations. This constraint is enforced using a Lagrange multiplier formulation. Analogous to the contact formulation, a Lagrange multiplier field  $\boldsymbol{\lambda}_*^{(i)}$  is introduced on the interface  $\Gamma_*^{(i)}$ . The resulting contributions to the total virtual work consist of the coupling interface term

$$-\delta\mathcal{W}_*^{(i)} = \int_{\Gamma_*^{(i)}} \boldsymbol{\lambda}_*^{(i)} \left( \delta\mathbf{u}^{(i,\mathcal{L})} - \delta\mathbf{u}^{(i,\mathcal{B})} \right) dA_0, \quad (34)$$

and the variational form of the coupling constraint

$$\delta\mathcal{W}_{\lambda_*^{(i)}} = \int_{\Gamma_*^{(i)}} \delta\lambda_*^{(i)} \left( \mathbf{u}^{(i,\mathcal{L})} - \mathbf{u}^{(i,\mathcal{B})} \right) dA_0. \quad (35)$$

With this, the mixed formulation of the embedded mesh problem reads: Find  $\mathbf{u}^{(i)} \in \mathcal{U}^{(i)}$  and  $\lambda_*^{(i)} \in \mathcal{L}$  such that

$$\delta\mathcal{W}_{\text{int,ext}} \left( \mathbf{u}^{(i)}, \delta\mathbf{u}^{(i)} \right) - \delta\mathcal{W}_*^{(i)} \left( \lambda_*^{(i)}, \delta\mathbf{u}^{(i)} \right) = 0 \quad \forall \delta\mathbf{u}^{(i)} \in \mathcal{V}^{(i)}, \quad (36)$$

$$\delta\mathcal{W}_{\lambda_*^{(i)}} \left( \mathbf{u}^{(i)}, \delta\lambda_*^{(i)} \right) = 0 \quad \forall \delta\lambda_*^{(i)} \in \mathcal{L}. \quad (37)$$

where  $\mathcal{L}$  is the dual space of the trace space of  $\mathcal{V}^{(i)}$  restricted to  $\Gamma_*^{(i)}$  [43].

### 3.3 Combined contact-embedded mesh formulation

The contact and embedded mesh coupling formulations are now combined to obtain a mixed finite element formulation in which the displacement field  $\mathbf{u}^{(i)}$ , the contact tractions  $\lambda$ , and the interface tractions  $\lambda_*^{(i)}$  are solved simultaneously. Incorporating the embedded mesh coupling contributions (34) and (35) into the contact problem defined by (27) and (28) yields the following weak formulation

$$-\delta\mathcal{W}_{\text{int,ext}} \left( \mathbf{u}^{(i)}, \delta\mathbf{u}^{(i)} \right) - \delta\mathcal{W}_{\text{co}} \left( \lambda, \delta\mathbf{u}^{(i)} \right) - \delta\mathcal{W}_*^{(i)} \left( \lambda_*^{(i)}, \delta\mathbf{u}^{(i)} \right) = 0 \quad \forall \delta\mathbf{u}^{(i)} \in \mathcal{V}^{(i)}, \quad (38)$$

$$\delta\mathcal{W}_\lambda \left( \mathbf{u}^{(i)}, \delta\lambda \right) \geq 0 \quad \forall \delta\lambda \in \mathcal{M}^+, \quad (39)$$

$$\delta\mathcal{W}_{\lambda_*^{(i)}} \left( \mathbf{u}^{(i)}, \delta\lambda_*^{(i)} \right) = 0 \quad \forall \delta\lambda_*^{(i)} \in \mathcal{L}. \quad (40)$$

Several key differences can be identified between the contact contributions (30) and (31) and the embedded mesh contributions (34) and (35). Due to the nature of contact problems, the contact terms depend on the current deformation of the bodies. Thus, the contact contributions are formulated in the current configuration, whereas the embedded mesh coupling terms are formulated in the reference configuration. Consequently, the projection  $\chi$  in (30) must be evaluated continuously to capture the relative motion between slave and master sides in the current configuration. In contrast, although a projection is also required for the embedded mesh contribution (34), it is evaluated only once in the reference configuration. Finally, the weak contact formulation (39) contains an inequality constraint, whereas the embedded mesh formulation (40) leads to an equality constraint. The inequality requires specialized numerical treatment, typically based on active-set strategies [64, 62, 12, 65].

## 4 Spatial discretization and numerical integration

In Section 2, the mesh generation workflow for the bodies involved in the contact problem was described, resulting in discretizations of the subdomains  $\Omega_0^{(i,\mathcal{L})}$  and  $\Omega_0^{(i,\mathcal{B})}$ . As introduced previously, the mesh associated with  $\Omega_0^{(i,\mathcal{L})}$  is referred to as the *boundary layer mesh*, whereas the mesh representing  $\Omega_0^{(i,\mathcal{B})}$  is referred to as the *background mesh*. Furthermore, in Section 3, a mixed finite element formulation was derived involving three unknown fields: the displacement  $\mathbf{u}^{(i)}$ , the contact tractions  $\lambda$ , and the embedded mesh interface tractions  $\lambda_*^{(i)}$ .

In the following, the spatial discretization of these fields is presented. We begin with the discretization of the subdomains  $\Omega_0^{(i,\mathcal{L})}$  and  $\Omega_0^{(i,\mathcal{B})}$ . Subsequently, a mortar finite element discretization is introduced for the Lagrange multiplier fields. First, the mortar discretization of the contact tractions  $\lambda$  is discussed, followed by that of the embedded mesh interface tractions  $\lambda_*^{(i)}$ . For the latter, particular attention is paid to the selection of suitable discrete Lagrange multiplier spaces.

The proposed discretization approach can be fully automated, as outlined in Section 2, where the process originates from an arbitrary NURBS-based surface representation defined in a CAD/CAM system. Following the meshing pipeline illustrated in Figure 5 leads to the mesh configuration shown in Figure 8, in which the boundary layer mesh overlaps the Cartesian background mesh. As a result, some elements of the background mesh are intersected by the coupling interface  $\Gamma_*$  of the boundary layer mesh. These intersected elements, referred to as *cut elements*, require special treatment in the numerical integration procedure. The corresponding treatment, together with additional details on the contact integration, is discussed at the end of this section.

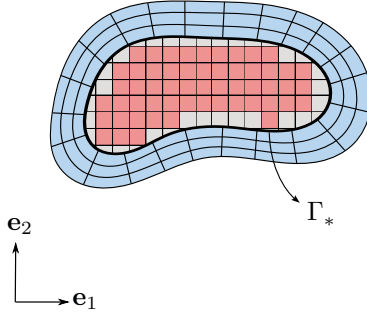


Figure 8: Spatial discretization approach. The boundary layer mesh and the background mesh are shown in blue and red, respectively. Background elements intersected by the coupling interface  $\Gamma_*$  are highlighted in gray.

**Remark 4.1.** For the discretization of the boundary layer and background meshes, both isogeometric and classical Lagrangian elements may be employed and combined arbitrarily. In isogeometric elements, the degrees of freedom are associated with control points, whereas in Lagrangian elements they are associated with nodes. For simplicity of terminology, both control points and nodes are hereafter collectively referred to as nodes.

#### 4.1 Structure discretization

The solid subdomains  $\Omega_0^{(i,\mathcal{L})}$  and  $\Omega_0^{(i,\mathcal{B})}$  are discretized using an isoparametric approach. For the subdomains  $j = \mathcal{L}, \mathcal{B}$ , the discrete element position  $\mathbf{X}_h^{(i,j)}$ , displacement  $\mathbf{u}_h^{(i,j)}$ , and virtual displacement  $\delta\mathbf{u}_h^{(i,j)}$  are approximated as

$$\mathbf{X}_h^{(i,j)} = \sum_{k=1}^{n^{(i,j)}} \Psi_k \mathbf{x}_k^{(i,j)}, \quad (41)$$

$$\mathbf{u}_h^{(i,j)} = \sum_{k=1}^{n^{(i,j)}} \Psi_k \mathbf{d}_k^{(i,j)}, \quad (42)$$

and

$$\delta\mathbf{u}_h^{(i,j)} = \sum_{k=1}^{n^{(i,j)}} \Psi_k \delta\mathbf{d}_k^{(i,j)}. \quad (43)$$

Here,  $\Psi_k \in \mathbb{R}$  denotes the interpolation function associated with element node  $k$ , while  $\mathbf{x}_k^{(i,j)}$ ,  $\mathbf{d}_k^{(i,j)}$ , and  $\delta\mathbf{d}_k^{(i,j)}$  represent the nodal positions, displacements, and virtual displacements, respectively. For body  $i$ , each subdomain  $j$  contains  $n^{(i,j)}$  nodes. The definition of the interpolation functions  $\Psi_k$  depends on the chosen discretization technology. Following the discretization workflow described in Section 2, the boundary layer domain  $\Omega_0^{(i,\mathcal{L})}$  is discretized using NURBS basis functions in order to ensure a  $C^1$ -continuous surface description, which is advantageous for the contact formulation. The background mesh  $\Omega_0^{(i,\mathcal{B})}$  may be discretized either by classical Lagrangian polynomials within the FEM framework or by NURBS basis functions within IGA.

#### 4.2 Discretization of the contact Lagrange multiplier

A mortar finite element discretization is applied to the contact traction  $\boldsymbol{\lambda}$ , see [12, 61]. The resulting discrete Lagrange multiplier field  $\boldsymbol{\lambda}_h$  is given by

$$\boldsymbol{\lambda}_h = \sum_{q=1}^m \Phi_q \boldsymbol{\lambda}_q. \quad (44)$$

Here,  $\Phi_q$  is a matrix of shape functions, and  $\boldsymbol{\lambda}_q$  represents the corresponding nodal Lagrange multipliers. In mortar discretizations, it is common that each node on the slave side carries a Lagrange

multiplier, i.e.,  $m = n_{sl}$ , where  $n_{sl}$  denotes the number of nodes on the slave side. However, this is not a strict requirement. For second-order Lagrangian elements, it is often preferable that not all slave-side nodes carry a Lagrange multiplier, i.e.,  $m < n_{sl}$ , see [14, 63].

In [66], a mortar framework based on dual shape functions (which will be briefly discussed in the following lines) was proposed for contact mechanics and classical domain decomposition for NURBS discretizations of second and third order. Optimal convergence rates under uniform mesh refinement were demonstrated. In the present approach, the contact surfaces are discretized using a boundary layer based on NURBS shape functions. Consequently, we follow the mortar discretization strategy of [66] and assign one scalar Lagrange multiplier to each slave-side node.

To complete the discretization, suitable shape functions for the Lagrange multiplier field  $\boldsymbol{\lambda}$  must be defined. We therefore introduce a discrete Lagrange multiplier space  $\boldsymbol{\mathcal{M}}_{c,h}^+$  that approximates the continuous space  $\boldsymbol{\mathcal{M}}^+$ . In mortar finite element discretizations, the selection of an appropriate discrete space for  $\boldsymbol{\mathcal{M}}_{c,h}^+$  is crucial to ensure stability of the method [62]. Two well-known types of Lagrange multiplier interpolation are *standard* and *dual* shape functions. For standard shape functions,  $\Phi_q$  are chosen identical to the shape functions used to interpolate the primal variable on the slave side  $\Gamma_c^{(1)}$ , i.e.,  $\Phi_q = \Psi_a$ . On the other hand, dual shape functions are constructed such that they satisfy the biorthogonality condition

$$\int_{\gamma_{c,h}^{(1)}} \Phi_q \Psi_a \, dA = \delta_{qa} \int_{\gamma_{c,h}^{(1)}} \Psi_a \, dA, \quad q, a = 1, \dots, m. \quad (45)$$

Here,  $\delta_{qa}$  denotes the Kronecker delta. Satisfaction of the biorthogonality condition ensures that the dual shape functions  $\Phi_q$  are well defined and possess the required approximation properties. Dual shape functions simplify the enforcement of mortar coupling conditions while preserving the mathematical properties of the method. Furthermore, they allow for efficient condensation of the discrete Lagrange multiplier degrees of freedom, thereby eliminating the saddle-point structure of the resulting system. For further details on the construction of dual shape functions, we refer to [67, 61].

Substituting (43) and (44) into the contact virtual work expression (30) yields the discretized contact virtual work

$$\begin{aligned} \delta \mathcal{W}_{co,h} &= \sum_{q=1}^m \sum_{a=1}^{n_{sl}} \boldsymbol{\lambda}_q^T \left( \int_{\gamma_c^{(1)}} \Phi_q \Psi_a \, dA \right) \delta \mathbf{d}_a^S \\ &\quad - \sum_{q=1}^m \sum_{b=1}^{n_{ma}} \boldsymbol{\lambda}_q^T \left( \int_{\gamma_c^{(1)}} \Phi_q (\Psi_b \circ \chi_h) \, dA \right) \delta \mathbf{d}_b^M, \end{aligned} \quad (46)$$

where,  $\delta \mathbf{d}_a^S$  and  $\delta \mathbf{d}_b^M$  denote the virtual displacements on the slave and master side, respectively. In the present formulation,  $\delta \mathbf{d}_a^S \in \delta \mathbf{d}_a^{(1,\mathcal{L})}$  and  $\delta \mathbf{d}_b^M \in \delta \mathbf{d}_b^{(2,\mathcal{L})}$ . The operator  $\chi_h : \gamma_{c,h}^{(2)} \rightarrow \gamma_{c,h}^{(1)}$  defines a suitable projection from the discretized master side onto the discretized slave side. The master side is described by  $n_{ma}$  number of nodes. From (46), the mortar matrices  $\mathbf{D}$  and  $\mathbf{M}$  are defined as

$$\mathbf{D}[q, a] = \int_{\gamma_c^{(1)}} \Phi_q \Psi_a \, dA \, \mathbf{I}, \quad q = 1, \dots, m, a = 1, \dots, n_{sl} \quad (47)$$

$$\mathbf{M}[q, b] = \int_{\gamma_c^{(1)}} \Phi_q (\Psi_b \circ \chi_h) \, dA \, \mathbf{I}, \quad q = 1, \dots, m, b = 1, \dots, n_{ma}, \quad (48)$$

where  $\mathbf{I} \in \mathbb{R}^{3 \times 3}$  denotes the identity matrix. In general, both  $\mathbf{D}$  and  $\mathbf{M}$  are rectangular matrices. However, if  $m = n_{sl}$ , the matrix  $\mathbf{D}$  becomes square. To simplify the notation, we can define a discrete displacement vector  $\mathbf{d}^{co}$ , which groups the displacements related to the contact interface in  $\mathbf{d}^{co} = (\mathbf{d}^M, \mathbf{d}^S)$ . Substituting the mortar matrices (47) and (48) into (46) yields

$$\begin{aligned} \delta \mathcal{W}_{co,h} &= \delta \mathbf{d}^{S^T} \mathbf{D}^T \boldsymbol{\lambda} - \delta \mathbf{d}^{M^T} \mathbf{M}^T \boldsymbol{\lambda} \\ &= \delta \mathbf{d}^{co^T} \underbrace{\begin{bmatrix} -\mathbf{M}^T \\ \mathbf{D}^T \end{bmatrix}}_{\mathbf{f}_{co}(\mathbf{d}^{co}, \boldsymbol{\lambda})} \boldsymbol{\lambda} = \delta \mathbf{d}^{co^T} \mathbf{f}_{co}(\mathbf{d}^{co}, \boldsymbol{\lambda}). \end{aligned} \quad (49)$$

Finally, the weak constraint contribution for frictionless contact, defined in (28) and (31), is discretized. In [68], the discrete counterpart of these expressions is derived and shown to be equivalent to pointwise conditions. The corresponding discrete conditions read

$$(\tilde{g}_n)_q \geq 0, \quad (\lambda_n)_q \geq 0, \quad (\tilde{g}_n)_q (\lambda_n)_q = 0, \quad q = 1, \dots, m, \quad (50)$$

where  $(\tilde{g}_n)_q$  denotes the discrete weighted gap function at the slave node  $q$ , defined by

$$(\tilde{g}_n)_q = \int_{\gamma_c^{(1)}} \Phi_q g_{n,h} \, dA, \quad (51)$$

with  $g_{n,h}$  representing the discretized gap function introduced in (21).

### 4.3 Discretization of the embedded mesh Lagrange multiplier

Analogously to the contact traction, the embedded mesh coupling traction  $\lambda_*^{(i)}$  is discretized using a mortar-based approach. Since this discretization is performed for each body  $i$ , the superscript  $(i)$  is omitted in the following for notational simplicity. For an arbitrary body, the discrete embedded mesh coupling traction is given by

$$\lambda_{*,h} = \sum_{r=1}^{m_*} \Phi_r^* \lambda_{*r}, \quad (52)$$

where  $\Phi_r^*$  denote the Lagrange multiplier shape functions, and  $\lambda_{*r}$  are the associated nodal Lagrange multipliers defined on the coupling interface  $\Gamma_*$ .

The selection of suitable Lagrange multiplier shape functions in (52) is more involved than in classical mesh-tying configurations. In standard mesh tying, two boundary-conforming meshes are coupled along a common interface. In contrast, in an embedded mesh configuration only one mesh—here, the boundary layer mesh—remains boundary conforming and defines the coupling interface, which is embedded into the second mesh, namely the Cartesian background mesh. As a consequence, stability properties that hold for commonly used Lagrange multiplier spaces in classical mortar methods do not automatically transfer to the embedded mesh setting. In particular, an inappropriate choice of the discrete Lagrange multiplier space may lead to an unstable multiplier field due to a violation of the discrete inf-sup condition [69].

In this work, the Lagrange multipliers are defined at the nodes on  $\Gamma_*$ , following the approach proposed in [42]. For an interface  $\Gamma_*$  described by the inner surface of the boundary layer mesh with  $n_*^{\mathcal{I}}$  nodes, this yields  $m_* = n_*^{\mathcal{I}}$ . Furthermore, a standard mortar interpolation is employed for the Lagrange multiplier field, i.e.,  $\Phi_r^* = \Psi_c$ , where  $\Psi_c$  denote the shape functions defining  $\Gamma_*$ .

As shown in [42], the use of Lagrange multiplier fields in embedded mesh configurations may lead to mesh locking if the overlapping mesh is finer and stiffer than the underlying mesh. It should be noted that alternative coupling strategies exist, such as Nitsche's method [70, 42, 40] and discontinuous Galerkin approaches [69, 71], which do not exhibit mesh locking and could be employed instead of a mortar-based formulation. Nevertheless, for the class of problems considered in this work, stable and convergent results can be achieved using a mortar-based approach. This is demonstrated by the numerical experiments presented in Subsections 5.2 and 5.4.

By inserting the approximations (43) and (52) into (34) and (35), the discretized coupling contributions are obtained as

$$-\delta \mathcal{W}_{*,h} = \sum_{c=1}^{n_*^{\mathcal{I}}} \sum_{r=1}^{m_*} \lambda_{*r}^{\mathcal{I}} \left( \int_{\Gamma_*} \Phi_r^* \Psi_c \, dA \right) \delta \mathbf{d}_c^{\mathcal{I}} - \sum_{d=1}^{n_*^{\mathcal{C}}} \sum_{r=1}^{m_*} \lambda_{*r}^{\mathcal{I}} \left( \int_{\Gamma_*} \Phi_r^* (\Psi_d \circ \chi_h^*) \, dA \right) \delta \mathbf{d}_d^{\mathcal{C}}, \quad (53)$$

and

$$\delta \mathcal{W}_{\lambda_{*,h}} = \sum_{c=1}^{n_*^{\mathcal{I}}} \sum_{r=1}^{m_*} \delta \lambda_{*r}^{\mathcal{I}} \left( \int_{\Gamma_*} \Phi_r^* \Psi_c \, dA \right) \mathbf{d}_c^{\mathcal{I}} - \sum_{d=1}^{n_*^{\mathcal{C}}} \sum_{r=1}^{m_*} \delta \lambda_{*r}^{\mathcal{I}} \left( \int_{\Gamma_*} \Phi_r^* (\Psi_d \circ \chi_h^*) \, dA \right) \mathbf{d}_d^{\mathcal{C}}, \quad (54)$$

where  $\delta \mathbf{d}_c^{\mathcal{I}}$  and  $\delta \mathbf{d}_d^{\mathcal{C}}$  denote the virtual displacements on the interface and on the corresponding cut elements of the background mesh, respectively, such that  $\delta \mathbf{d}_c^{\mathcal{I}} \in \delta \mathbf{d}_c^{\mathcal{L}}$  and  $\delta \mathbf{d}_d^{\mathcal{C}} \in \delta \mathbf{d}_d^{\mathcal{B}}$ . Furthermore,  $n_*^{\mathcal{C}}$  is the number of nodes associated with the corresponding cut elements. The operator  $\chi_h^* : \Gamma_{*,h}^{\mathcal{I}} \rightarrow \Gamma_{*,h}^{\mathcal{C}}$  defines a projection mapping a point on the boundary layer interface to a corresponding point in the background mesh. It is important to emphasize that the projection operator  $\chi_h^*$  differs fundamentally from the contact projection  $\chi_h$  introduced in (46). While  $\chi_h^*$  defines a *surface-to-volume* projection,  $\chi_h$  corresponds to a *surface-to-surface* projection. This distinction reflects a fundamental difference between

mortar formulations for embedded mesh coupling and those used in contact problems, with significant implications for the evaluation of discrete projections, mesh intersection procedures, and the required geometric operations. Based on (53) and (54), the mortar matrices  $\mathbf{D}_*$  and  $\mathbf{M}_*$  are defined by

$$\mathbf{D}_*[r, c] = \int_{\Gamma_*} \Phi_r^* \Psi_c \, dA \, \mathbf{I}, \quad r = 1, \dots, m_*, c = 1, \dots, n_*^{\mathcal{I}}, \quad (55)$$

$$\mathbf{M}_*[r, d] = \int_{\Gamma_*} \Phi_r^* (\Psi_d \circ \chi_h^*) \, dA \, \mathbf{I}, \quad r = 1, \dots, m_*, d = 1, \dots, n_*^{\mathcal{C}}. \quad (56)$$

Similar to the previous subsection, the notation can be simplified by defining a discrete displacement vector  $\mathbf{d}^* = (\mathbf{d}^{\mathcal{C}}, \mathbf{d}^{\mathcal{I}})$ , which collects the displacements associated with the embedded mesh coupling. Using the mortar matrices  $\mathbf{D}_*$  and  $\mathbf{M}_*$ , we can reformulate (53) and (54), which yields

$$-\delta \mathcal{W}_{*,h} = \delta \mathbf{d}^{\mathcal{I}\top} \mathbf{D}_*^{\top} \boldsymbol{\lambda}_* - \delta \mathbf{d}^{\mathcal{C}\top} \mathbf{M}_*^{\top} \boldsymbol{\lambda}_* = \delta \mathbf{d}^{*\top} \underbrace{\begin{bmatrix} -\mathbf{M}_*^{\top} \\ \mathbf{D}_*^{\top} \end{bmatrix}}_{\mathbf{f}_*(\boldsymbol{\lambda}_*)} \boldsymbol{\lambda}_* = \delta \mathbf{d}^{*\top} \mathbf{f}_*(\boldsymbol{\lambda}_*), \quad (57)$$

and

$$\delta \mathcal{W}_{\lambda_*,h} = \delta \boldsymbol{\lambda}_*^{\top} \mathbf{D}_* \mathbf{d}^{\mathcal{I}} - \delta \boldsymbol{\lambda}_*^{\top} \mathbf{M}_* \mathbf{d}^{\mathcal{C}} = \delta \boldsymbol{\lambda}_*^{\top} \underbrace{\begin{bmatrix} -\mathbf{M}_* & \mathbf{D}_* \end{bmatrix}}_{\mathbf{g}_*(\mathbf{d}^*)} \mathbf{d}^*. \quad (58)$$

Here,  $\mathbf{f}_*$  represents the vector of discretized forces acting on the degrees of freedom (DOFs) involved in the embedded mesh coupling, including both interface and cut element nodes. The vector  $\mathbf{g}_*$  denotes the discrete coupling constraint.

#### 4.4 Complete discretized contact-embedded mesh formulation

Finally, all discretized residual contributions from the internal and external forces, as well as from the contact and embedded mesh coupling formulations, are assembled into the global weak formulation introduced in (38)–(40). To this end, we define the global displacement vector  $\mathbf{d} = (\mathbf{d}^{\mathcal{N}}, \mathbf{d}^{\mathcal{C}}, \mathbf{d}^*)$ , where  $\mathbf{d}^{\mathcal{N}}$  groups the remaining displacements that are not associated with the contact or embedded mesh coupling formulations. The discretized problem formulation reads

$$\mathbf{f}_{\text{int}}(\mathbf{d}) + \mathbf{f}_{\text{co}}(\mathbf{d}, \boldsymbol{\lambda}) + \mathbf{f}_*(\boldsymbol{\lambda}_*) - \mathbf{f}_{\text{ext}} = \mathbf{0}, \quad (59)$$

$$(\tilde{g}_n)_q \geq 0, \quad (\lambda_n)_q \geq 0, \quad (\tilde{g}_n)_q (\lambda_n)_q = 0, \quad q = 1, \dots, m, \quad (60)$$

$$\mathbf{g}_*(\mathbf{d}) = \mathbf{0}. \quad (61)$$

The resulting nonlinear system is solved using the Newton-Raphson method. The system exhibits a double saddle-point structure due to the mixed formulation for both the contact and embedded mesh coupling. In the following, we briefly describe the solution strategies to solve the nonlinear and linear systems.

The inequality constraint in (60) introduces an additional nonlinearity, since the active set of slave nodes in contact with the master side is not known a priori. To address this, a primal-dual active set strategy (PDASS) is employed within the contact solution algorithm. In short, the PDASS can be interpreted as a semismooth Newton method [72], which treats the nonlinearities arising from finite deformations, nonlinear material behaviour, and contact within a unified iterative scheme. This requires a reformulation of the KKT conditions using a nonlinear complementarity function  $C_j$  for each slave node  $j$ . Results from the mathematical literature show that the resulting formulation is semismooth, such that a Newton method can still be applied. Furthermore, the algorithm requires a consistent linearization of all deformation-dependent contact quantities, such as the mortar matrices  $\mathbf{D}$  and  $\mathbf{M}$ . The algorithmic details of the PDASS and the consistent linearization of deformation-dependent contact terms are described in [73, 12, 65, 62].

Although the saddle-point system in (59)–(61) can be solved using either direct solvers or tailored iterative solvers, some techniques may be employed to simplify the system. For the contact block, the use of dual shape functions for the interpolation of the Lagrange multipliers is particularly advantageous. The biorthogonality property reduces the mortar matrix  $\mathbf{D}$  to a diagonal matrix, which enables straightforward elimination of the discrete Lagrange multipliers by static condensation [61, 12, 65, 73, 63].

To eliminate the Lagrange multipliers in the embedded mesh coupling problem, a node-wise penalty regularization is introduced [74, 75, 76, 77]. The regularization reads

$$\boldsymbol{\lambda}_* \approx \epsilon \boldsymbol{\kappa}^{-1} \mathbf{g}_* (\mathbf{d}^*), \quad (62)$$

thus, the Lagrange multiplier  $\boldsymbol{\lambda}_*$  becomes a pure function of the unknown displacements  $\mathbf{d}^*$ . Here,  $\epsilon \in \mathbb{R}^+$  denotes the penalty parameter, and  $\boldsymbol{\kappa}$  is a diagonal nodal scaling matrix. An exact fulfillment of (62) is achieved for  $\epsilon \rightarrow \infty$ , which, however, leads to poor conditioning of the system. For practical purposes, a penalty parameter of the order  $\epsilon \sim 100 E$  has proven sufficiently accurate, where  $E$  denotes the Young's modulus of the material. The contribution of the discrete coupling constraint  $\mathbf{g}_*$  is proportional to the support of the associated Lagrange multiplier shape functions; i.e., it depends on the interface element area. As described in [75], to ensure the fulfillment of the patch tests presented in Subsection 5.1, the vector  $\mathbf{g}_*$  is scaled by the inverse of the diagonal matrix  $\boldsymbol{\kappa}$ , following the approach presented in [74]. For each Lagrange multiplier node  $r$ , the local scaling matrix is defined as

$$\boldsymbol{\kappa}[r, r] = \int_{\Gamma_{*,h}} \Phi_r^* \, dA \, \mathbf{I}^{3 \times 3}, \quad (63)$$

which is assembled into the global scaling matrix  $\boldsymbol{\kappa}$ .

## 4.5 Numerical integration

Special attention is required for the numerical integration of the individual blocks arising from the contact and embedded mesh formulations. Focusing first on the contact contributions, the mortar matrices  $\mathbf{D}$  and  $\mathbf{M}$ , introduced in (47) and (48), respectively, require integration over the current slave side. To this end, a projection between the discretized master and slave sides is performed in order to determine suitable integration points. Established algorithms, such as integration schemes based on segmentation procedures, can be employed for this purpose. Such approaches have been successfully applied in contact formulations based on classical finite elements [9, 78, 65], as well as in contact problems using IGA discretizations [79, 80, 66].

The embedded mesh discretization illustrated in Figure 8 requires modifications to the element quadrature routines for cut elements that are overlapped by the boundary layer mesh. Moreover, within the embedded mesh formulation, the mortar matrices defined in (55) and (56) require integration over the coupling interface  $\Gamma_{*,h}$ . Such modifications are well established in the context of extended finite element methods (XFEM) [81, 38] and CutFEM approaches [32, 82]. In this work, we adopt the well-tested routines presented in [36, 83], which are briefly summarized in the following.

In Figure 9a, a two-dimensional cut element is intersected by the interface  $\Gamma_{*,h}$ . Two subdomains can be distinguished: a void region, which does not contribute to the element stiffness, and a material region, which does contribute to the stiffness. This decomposition requires computing the geometric intersection between the cut element and the interface. Since the interface  $\Gamma_{*,h}$  is represented by a nonlinear NURBS geometry, it is first subdivided into linear segments, yielding a linearized interface denoted by  $\Gamma_{*,h}^{\text{lin}}$ . The cut element is then intersected with these linear segments and partitioned into integration cells using a constrained Delaunay triangulation. For a two-dimensional element, the material part of the cut element is decomposed into triangular subcells. Each subcell is integrated using standard Gauss quadrature with  $n_{gp}$  Gauss points and corresponding weights, as illustrated in Figure 9b.

For the evaluation of the surface terms in the embedded mesh coupling, an integration rule must be defined on each interface element and its corresponding underlying cut element. This is achieved using the boundary segments obtained from the Delaunay triangulation. On these boundary segments, Gauss integration points are defined. The boundary segments and their associated Gauss points are then mapped onto the interface  $\Gamma_{*,h}$ , as illustrated in Figure 9c. In a final step, the integration points on  $\Gamma_{*,h}$  are then mapped to the background element.

## 5 Numerical examples

In this section, we present several numerical examples to validate the proposed discretization approach. Table 5 illustrates how the algorithmic building blocks are validated through these examples. Section 5.1 presents patch tests that verify the consistency of the embedded mesh coupling between the boundary layer and the background meshes. In Section 5.2, the applicability of the mortar-based method, described in Section 4.3, is demonstrated using the numerical example from [42, Section 7]. Section 5.3 investigates

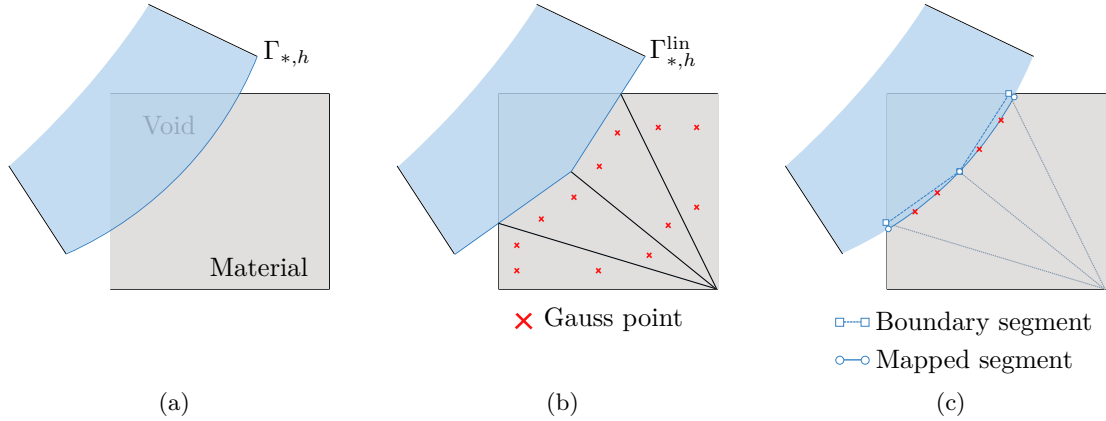


Figure 9: (a) Numerical integration of a cut element (gray) intersected by  $\Gamma_{*,h}$  (blue). (b) Resulting triangulation and Gauss points with the linearized interface  $\Gamma_{*,h}^{lin}$  (figure adapted from [42]). (c) Mapping of boundary segments and their Gauss points onto  $\Gamma_{*,h}$  and into the cut element.

the accuracy of the embedded mesh discretization in a contact problem through a spatial convergence study. Section 5.4 then presents a two-dimensional Hertzian contact problem. Finally, Section 5.5 demonstrates the approach in a three-dimensional setting, showcasing dynamic impact between two tori. For the numerical examples related to contact, the mortar finite element approach based on dual shape functions for NURBS discretizations presented in [66] was used.

The isogeometric B-reps are defined using the open-source library NURBS-Python [84]. Offset generation and preprocessing for all numerical examples are carried out with the open-source finite element pre-processor BeamMe [85]. The simulations are performed using the open-source multi-physics research code 4C [86].

Table 5: Validation of the algorithmic building blocks.

<b>Embedded mesh</b>	5.1 Patch test
	5.2 Mesh locking
<b>Embedded mesh with contact</b>	5.3 Convergence study
	5.4 Hertzian contact problem
	5.5 Two tori impact

## 5.1 Patch test

Patch tests are widely used to assess the consistency of finite element discretizations. A patch test is considered successful if an arbitrary patch is able to reproduce a state of constant stress [87, 88]. In this work, we consider the patch test shown in Figure 10, which consists of an elastic block ( $E = 1$ ,  $\nu = 0.3$ ) subjected to a uniform pressure load  $p = -0.01$  in  $y$ -direction. The continuum is described using nonlinear kinematics. The penalty parameter is set to  $\epsilon = 1000$ , and the width and height of the block are both  $a = 3$ . Although the problem is presented in a two-dimensional setting, it can be straightforwardly extended to three dimensions, as repeatedly demonstrated by the authors for similar contact and mesh coupling scenarios [63, 89]. To assess the consistency of the proposed methodology, the following representative mesh configurations are analyzed (see Figure 11):

- (a) boundary layer with straight interfaces,
- (b) boundary layer with inclined interfaces,
- (c) boundary layer with curved interfaces.

For all three configurations, a linear displacement field  $u_Y$  is obtained, as illustrated in Figure 12. Figure 13 shows the results of the Cauchy stress field  $\sigma_{Y\gamma}$  for the three configurations. The exact

fulfillment of the patch test is observed for the first and second configurations (Figures 13a and 13b, respectively), where a constant stress field is recovered up to machine precision. These results confirm the consistency of the proposed approach for coupling isogeometric and Cartesian meshes. The third configuration exhibits deviations of less than 1.6% in the element-wise stress field, which are localized to background elements intersected by the curved interfaces, as shown in Figure 13c. This behavior is expected, since the numerical integration described in Subsection 4.5 produces geometrically inexact integrations cells of the actual material domain for curved cutting interfaces [89, 83, 75, 77].

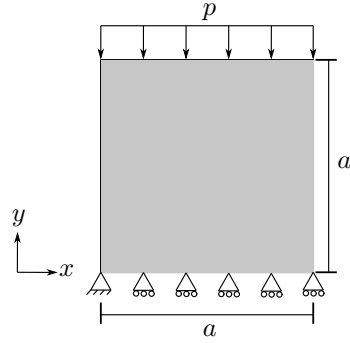


Figure 10: Problem setup of the patch test.

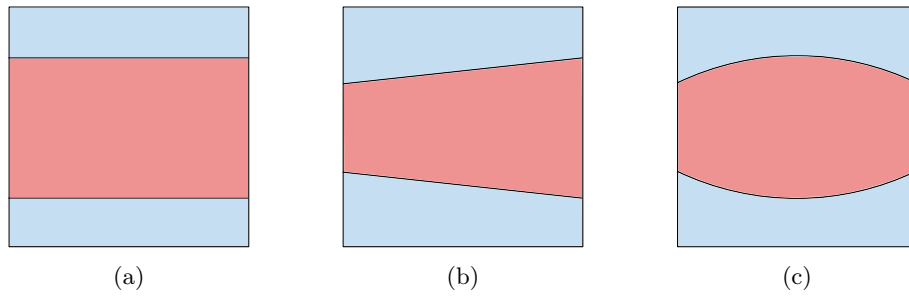


Figure 11: Mesh configurations used for the patch test: (a) straight interfaces, (b) inclined interfaces and (c) curved interfaces.

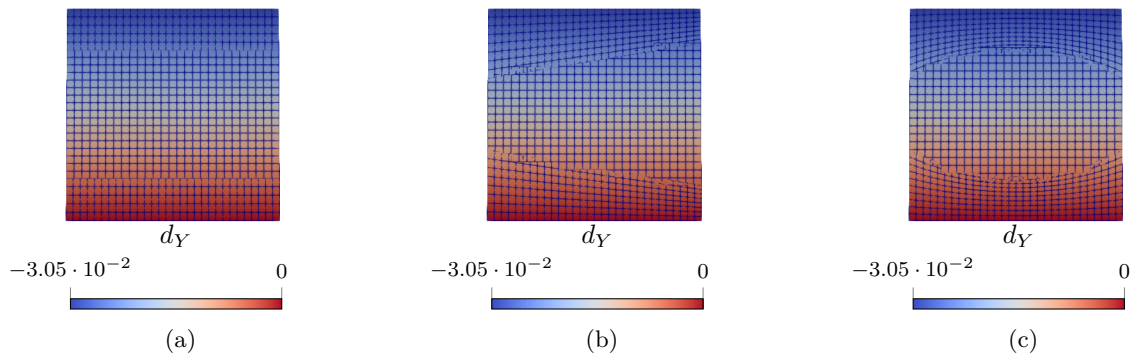


Figure 12: Displacement field  $u_Y$  of the patch tests: (a) straight interfaces, (b) inclined interfaces and (c) curved interfaces.

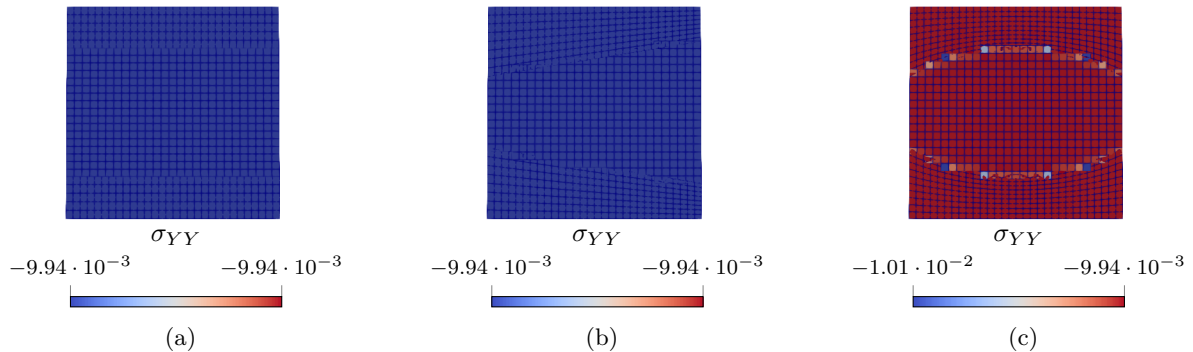


Figure 13: Cauchy stress  $\sigma_{YY}$  of the patch tests: (a) straight interfaces, (b) inclined interfaces and (c) curved interfaces.

## 5.2 Mesh locking

The mortar method in embedded mesh applications is known to potentially exhibit mesh-locking effects under specific conditions. The most critical configuration occurs when a fine mesh overlays a coarse mesh and the stiffness of the fine mesh is significantly higher than that of the coarse mesh [42]. In the present application, however, this issue is not expected, since the discretized bodies are assumed to possess homogeneous material properties. Consequently, the overlapping meshes share identical material parameters. Nevertheless, the potential occurrence of mesh locking is investigated in the following example.

We consider a problem setup similar to that presented in [42, Section 7]; see Figure 14a. The configuration consists of a two-dimensional, linear-elastic beam with dimensions  $l = 1.5$  and  $h = 1.0$ . A bending moment  $M$  is applied at both ends of the beam, induced by a linearly varying distribution of normal forces  $p(y) = -0.2y$ . Since the loading results in pure bending, the Cauchy stress component  $\sigma_{XX}$  is expected to vary linearly in the  $y$ -direction and to be independent of the beam stiffness. Figure 14b shows the analytical reference solution obtained using a highly refined mesh.

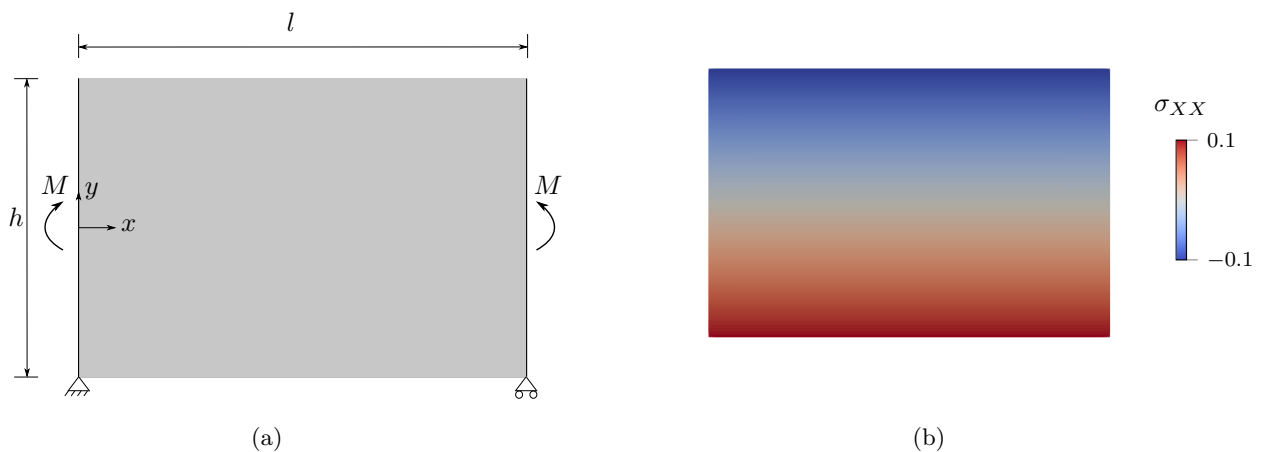


Figure 14: (a) Boundary conditions for bending beam and (b) its analytical reference solution.

For the mesh-locking study, the beam is discretized using two overlapping meshes, denoted as  $\Omega^{(\mathcal{L})}$  and  $\Omega^{(\mathcal{B})}$ . The interface  $\Gamma^*$  of  $\Omega^{(\mathcal{L})}$  is located at  $x = 0.625$  (Figure 15). The foreground mesh  $\Omega^{(\mathcal{L})}$  is discretized using NURBS elements of size  $h^{(\mathcal{L})}$ , while the background mesh  $\Omega^{(\mathcal{B})}$  consists of linear triangular and quadrilateral Lagrangian elements of size  $h^{(\mathcal{B})}$ . As suggested in [42, Section 7], the background mesh is arranged in a cross-hatched pattern to represent a worst-case configuration, in which the interface  $\Gamma^*$  diagonally intersects several background elements. Both meshes share identical material parameters,  $E_1 = E_2 = 50$  and  $\nu = 0.0$ . The coupling constraint, enforced by Lagrange multipliers, is applied along the interface  $\Gamma^*$ , and the penalty parameter is set to  $\epsilon = 10^6$ .

Two configurations are considered:

1. the foreground and background mesh elements are of comparable size, with  $h^{(\mathcal{B})}/h^{(\mathcal{L})} \approx 1.2$ ,

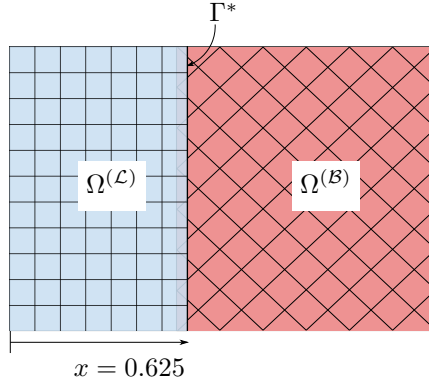


Figure 15: Discretization of the bending beam with overlapping NURBS (blue) and Lagrange (red) meshes.

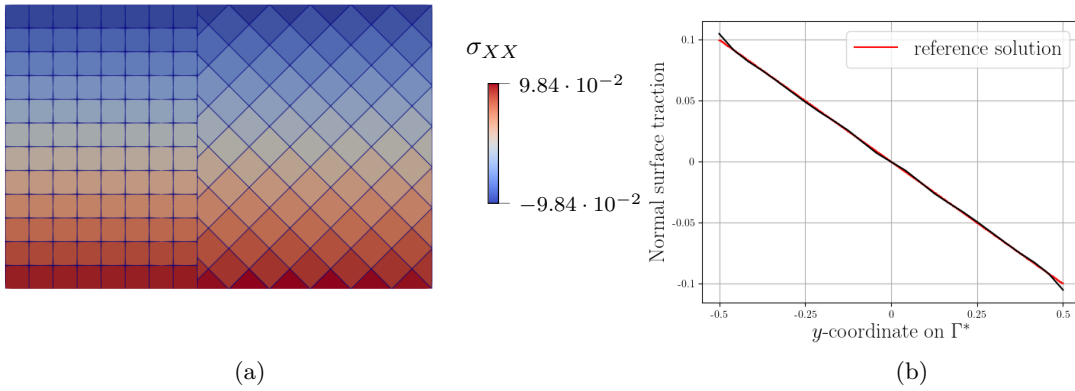


Figure 16: Results for configuration 1: (a) Cauchy stresses  $\sigma_{XX}$  on the beam. (b) Normal surface tractions on the interface  $\Gamma^*$ .

- the foreground mesh elements are finer than the background mesh elements, with  $h^{(\mathcal{B})}/h^{(\mathcal{L})} \approx 4.2$ .

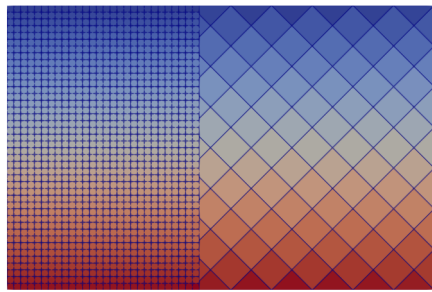
These configurations are motivated by contact applications, in which the isogeometric boundary layer mesh might be refined to accurately resolve contact interactions. For the first configuration, the computed stress  $\sigma_{XX}$  and the normal interface tractions exhibit very good agreement with the reference solution (Figure 16). In the second configuration, oscillations in the normal interface tractions are observed near the intersections of the interface  $\Gamma^*$  with the edges of the cut elements. These results are consistent with those reported in [42, Section 7]. The observed oscillations remain small and localized, showing that the adopted embedded mesh approach is suitable for the intended setting of overlapping meshes with identical material properties.

Although not directly relevant to our application, a third configuration is included for completeness. This configuration uses the same mesh ratio as the second configuration, with the difference that the NURBS mesh presents a significantly higher stiffness than the background mesh, namely  $E_1 = 50000$  and  $E_2 = 50$ . As expected, mesh locking is observed (Figure 18), characterized by significant stress fluctuations in the elements of the isogeometric boundary layer near the interface  $\Gamma^*$ .

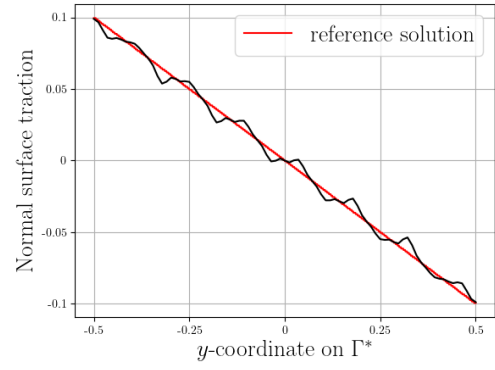
### 5.3 Convergence study in a contact problem

In this example, we investigate the spatial convergence of the proposed discretization approach applied to a contact problem. Figure 19a shows the boundary conditions of a simple two-dimensional contact problem between a linear-elastic block ( $E = 1$ ,  $\nu = 0$ ) and a rigid surface. The block has a width and height of  $w = h = 3$ . A distributed force  $f_y = 0.1x^4$  is applied to press the block against the rigid surface. Furthermore, the block is constrained to eliminate rigid body modes.

The block's domain is subdivided as shown in Figure 19b. Although the proposed discretization method generates  $\Gamma_*$  through an offset operation, in this example it is prescribed as an arbitrary curved

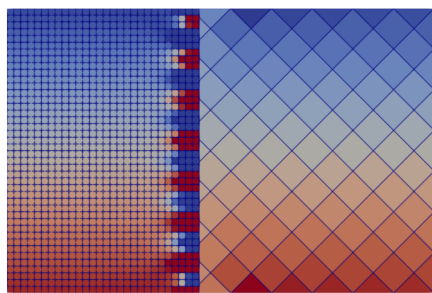


(a)

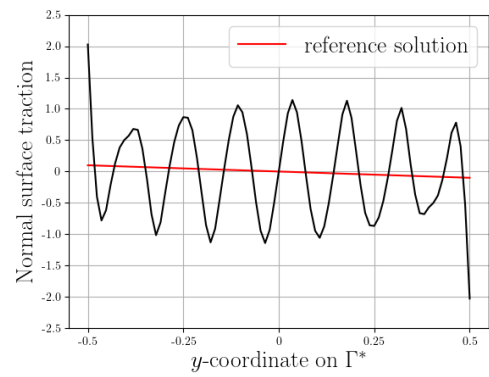


(b)

Figure 17: Results for configuration 2: (a) Cauchy stresses  $\sigma_{XX}$  on the beam. (b) Normal surface tractions on the interface  $\Gamma^*$ .



(a)



(b)

Figure 18: Results for configuration 3: (a) Cauchy stresses  $\sigma_{XX}$  on the beam. (b) Normal surface tractions on the interface  $\Gamma^*$ .

interface. This choice is made to verify the method in a more complex cut scenario. The NURBS patch representing the boundary layer is then constructed to conform to the contact interface and the curved boundary layer. The rigid surface is discretized using a second-order NURBS patch, while the background domain is discretized with a Cartesian mesh. For the contact boundary conditions, the slave side corresponds to the base of the block, whereas the master side is defined on the rigid surface. The penalty parameter associated with the embedded mesh formulation is set to  $\epsilon = 10^4$ .

Two mesh configurations are considered:

1. The boundary layer and background domains are discretized using second-order NURBS (*nurbs9*) and first-order Lagrangian elements (*quad4*), respectively
2. The boundary layer and background domains are discretized using second-order NURBS (*nurbs9*) and second-order serendipity Lagrangian elements (*quad8*), respectively.

The reference solution is obtained from a numerical simulation using a fine mesh size ( $h_{\text{ref}} = 2.344 \times 10^{-2}$ ), employing second-order NURBS for the boundary layer and second-order Lagrangian elements for the background mesh.

For this problem, the contact boundary does not evolve during deformation. As a result, optimal convergence rates in the energy norm are observed for both mesh configurations, as shown in Figure 20. In the first configuration, although the overlapping mesh is discretized using second-order NURBS, the convergence rate is limited to  $\mathcal{O}(h^1)$  due to the use of linear Lagrangian elements in the background mesh. In contrast, the second configuration achieves the optimal convergence rate of  $\mathcal{O}(h^2)$  by employing second-order Lagrangian elements in the background mesh. These results demonstrate that the proposed discretization approach effectively exploits the properties of both discretizations: the high-order continuity of the isogeometric boundary layer for the contact formulation and the mesh flexibility of independent background meshes, without compromising optimal spatial convergence.

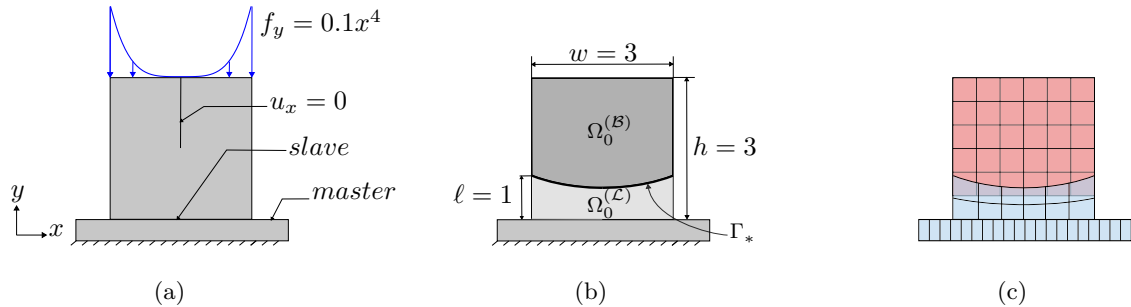


Figure 19: Contact problem between a block and a rigid surface. (a) Boundary conditions. (b) Subdivision of block's domain. (c) Discretization of the domains with NURBS (blue) and Lagrange elements (red).

## 5.4 Hertzian contact problem

To further demonstrate the capabilities of the proposed workflow, we consider a classical benchmark in contact mechanics: the Hertzian contact problem. In the two-dimensional configuration studied here, a linear-elastic half-cylinder ( $E = 250$ ,  $\nu = 0.0$ ) with radius  $R = 10$  is compressed against a rigid plate under a constant pressure  $p$ ; see Figure 21a. For this problem, an analytical expression for the normal contact traction  $p_c$  within the contact zone can be derived under the assumption of small deformations, c.f. [90]. The linear Hertzian solution is given by

$$p_c = \frac{4Rp}{\pi b^2} \sqrt{b^2 - x^2} \quad \text{with} \quad b = 2\sqrt{\frac{2R^2p(1-\nu^2)}{E\pi}}, \quad (64)$$

where  $b$  denotes the width of the contact zone. The maximum normal contact traction  $p_{c,\text{max}}$  occurs at  $x = 0$ .

It should be noted that the employed numerical contact formulation fully accounts for deformation-dependent nonlinearities. Therefore, an exact match between the numerical solution (which incorporate nonlinear effects) and the Hertzian solution (which is strictly based on linear kinematics) cannot be expected.

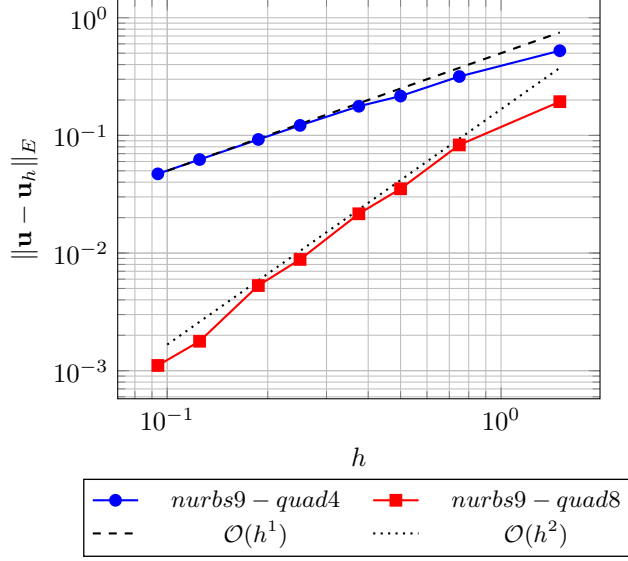


Figure 20: Convergence rates of two mesh configurations for the contact problem with embedded mesh discretization.

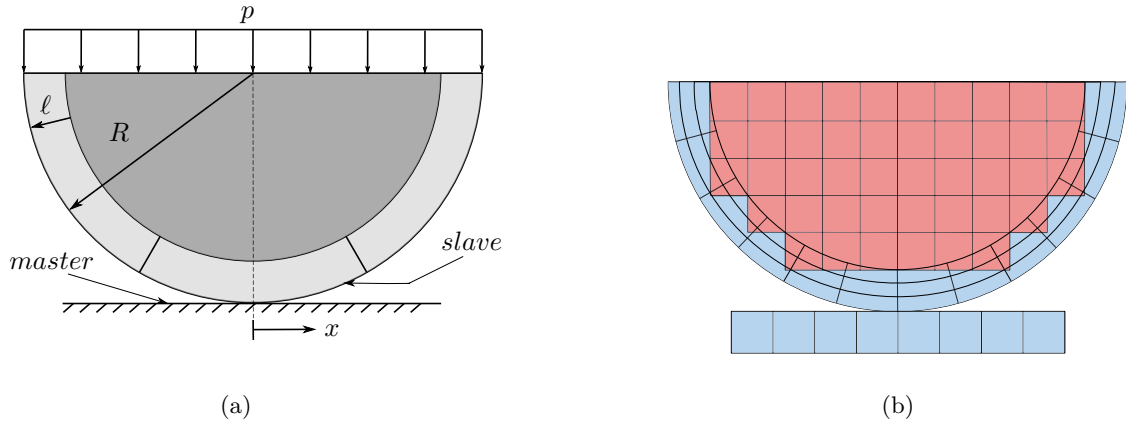


Figure 21: Hertzian contact problem. (a) Boundary conditions and subdivision of half-cylinder domain. (b) Discretization of the domains with NURBS (blue) and Lagrange elements (red).

Applying the proposed discretization approach, the half-cylinder domain is subdivided into a NURBS boundary layer with an offset thickness of  $\ell = 0.1$  and a bulk domain, as shown in Figure 21a. The boundary layer is discretized using second-order NURBS shape functions, while the background domain is discretized with a Cartesian mesh composed of Lagrangian elements (Figure 21b). The surface of the half-cylinder is defined as the slave interface, whereas the rigid plate acts as the master interface. For the embedded mesh coupling, the penalty parameter is set to  $\epsilon = 10^4$ .

The mesh generation process is illustrated in Figure 22. The procedure starts from the base B-rep, which in this case consists of three NURBS curve segments representing the potential contact boundary of the half-cylinder. These curves are offset by the distance  $\ell$ , generating three NURBS surface patches. Finally, the remaining bulk domain of the half-cylinder is discretized using a Cartesian mesh.

The spatial convergence of the numerical solution for  $p_{c,\max}$  is investigated using uniform mesh refinement for the load cases  $p = 0.3$  and  $p = 0.5$ . The corresponding results are presented in Figure 23. For both load levels, the solution converges to a stable value, exhibiting a consistent convergence trend under mesh refinement. As discussed above, a deviation from the Hertzian solution, which is based on linear theory, is expected. This discrepancy becomes less pronounced at lower load levels. Figure 24 depicts the contact traction  $p_c$  obtained on the finest mesh for  $p = 0.3$ , plotted along the radial coordinate of the half-cylinder. The numerical results show very close agreement with the Hertzian solution in terms of the traction distribution.

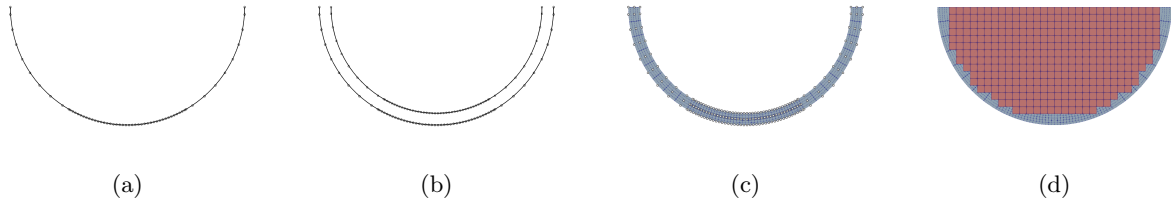


Figure 22: Mesh generation of a Hertzian contact problem: (a) base B-rep of half-cylinder, (b) offset of base B-rep, (c) NURBS boundary layer mesh, (d) discretization of bulk domain with a Cartesian mesh.

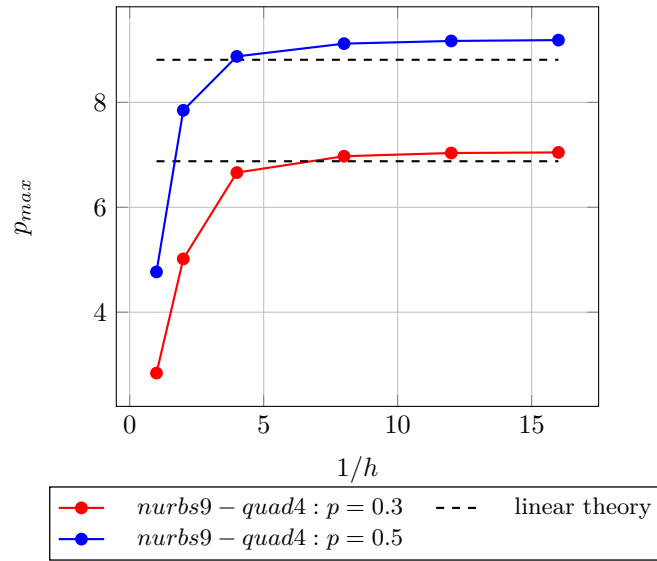


Figure 23: Spatial convergence of the Hertzian contact problem for the load cases  $p = 0.3$  and  $p = 0.5$ .

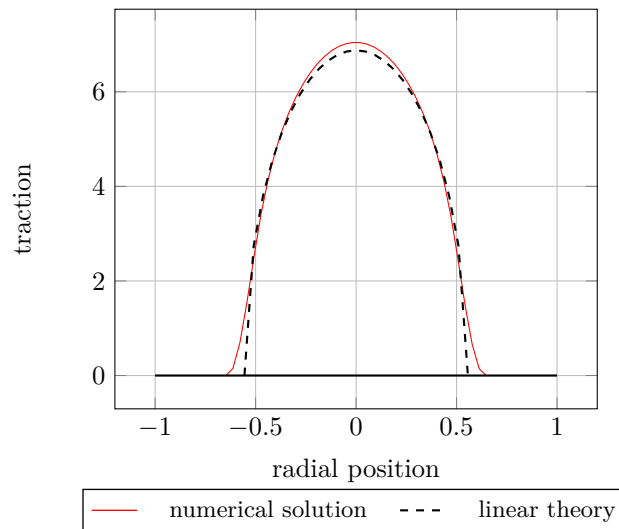


Figure 24: Traction along the contact interface for  $p = 0.3$ : comparison between the numerical solution on the finest mesh and the linear theory.

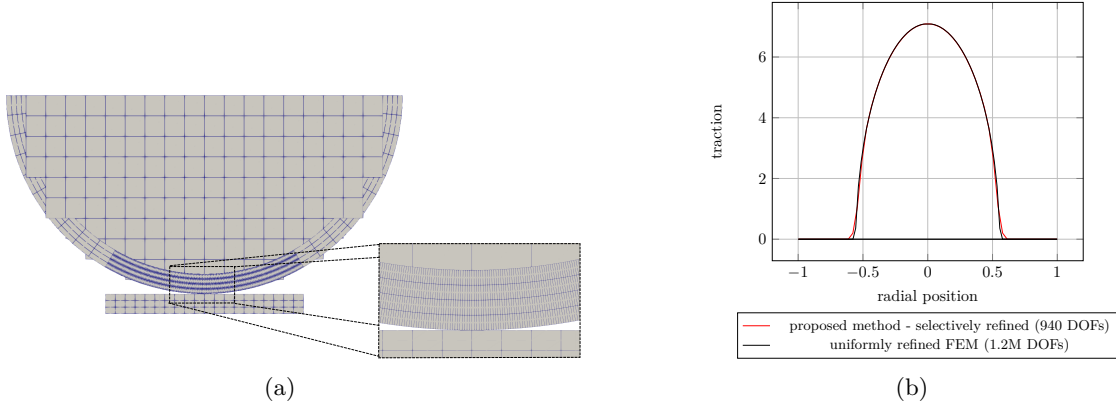


Figure 25: Demonstration of selective mesh refinement for the Hertzian contact problem: (a) locally refined boundary layer mesh; (b) resulting contact traction compared to a uniformly refined Lagrangian reference solution.

With this example, we further demonstrate the capabilities of the proposed discretization workflow, in particular its ability to selectively refine the boundary layer mesh independently of the bulk mesh while exploiting the high accuracy of NURBS discretizations in the contact region. To improve the contact stress solution, mesh refinement via knot insertion is applied exclusively to the central patch of the boundary layer. For the given boundary conditions and load  $p = 0.3$ , the side patches are not expected to come into contact with the rigid plate; refinement in these regions is therefore unnecessary. Since refinement of the bulk domain does not necessarily enhance the solution quality at the contact interface, the Cartesian mesh can remain relatively coarse. With this strategy, the final mesh consists of 768 DOFs in the central patch, 132 DOFs in each side patch, and 332 DOFs in the Cartesian mesh, resulting in a total of 1364 DOFs. The resulting mesh configuration is shown in Figure 25a. The contact tractions obtained with the selectively refined mesh are compared to those computed using a uniformly refined Lagrangian mesh with more than 1.3 million DOFs (Figure 25b), showing excellent agreement. These results highlight that the proposed discretization approach combines flexibility in mesh generation with high accuracy in the computed contact stresses.

## 5.5 Two tori in contact

The final numerical example demonstrates the applicability of the proposed discretization workflow to a three-dimensional time-dependent contact problem. The configuration is inspired by the example presented in [91], in which two hollow tori collide. In the present study, both tori are not hollow, but modeled as solid bodies. Each torus is described by a Neo-Hookean material model ( $E = 40$ ,  $\nu = 0.1$ ,  $\rho = 0.1$ ) and has major and minor radii of 1.5 and 0.5, respectively. The boundary layer thickness is  $\ell = 0.1$ . The centers of the first and second torus are located at  $O_{T_1} = (0, 0, 0)$  and  $O_{T_2} = (-0.5, 0, 0)$ , respectively. The axis of rotation of the first torus is defined by the unit vector  $\mathbf{a}_{T_1} = 1/\sqrt{2}(-1, 1, 0)$ , while the axis of rotation of the second torus is the  $z$ -axis. This configuration is shown in Figure 26a.

For each body, the spatial discretization consists of a NURBS boundary layer with 49,248 DOFs, while the Cartesian background mesh is composed of linear Lagrangian elements with 22,221 DOFs, resulting in a total of 142,932 DOFs for the two-body system. The penalty parameter is set to  $\epsilon = 1000$ . Time integration is performed using the generalized- $\alpha$  method with a spectral radius of  $\rho_\infty = 0.9$ . The simulation is carried out up to  $t = 5$  using a constant time step of  $\Delta t = 0.01$ .

Both bodies move toward each other with an initial velocity of  $v_0 = 0.162$ . It is well known that cut elements with very small integration volumes may lead to ill-conditioned systems and, consequently, convergence difficulties. To prevent this, cut elements with an integration volume smaller than a carefully chosen threshold tolerance are removed.

Characteristic deformation stages during contact are shown in Figure 26. To improve visualization of the boundary layer and Cartesian meshes, the discretization is intersected with the  $xy$ -plane, providing a side view of the deformed configuration, c.f. Figure 27. The results illustrate large deformations and significant sliding between the tori, benefiting from the  $C^1$  continuity of the isogeometric boundary layer discretization. Overall, this example demonstrates the applicability of the proposed approach to complex three-dimensional contact problems involving large deformations, highlighting its potential for even more

demanding realistic scenarios.

## 6 Conclusion

In this work, we proposed a novel discretization approach for contact problems with NURBS boundary layers and presented the algorithmic building blocks of the method. Starting from the mesh generation, a simplified strategy was introduced based on the construction of a boundary layer mesh that contains the NURBS B-rep representation of the contact body. The remaining bulk domain of the contact body is described by a nonconforming Cartesian background mesh. This results in a configuration in which the boundary layer mesh overlaps the background discretization. Although several techniques can be employed to generate the boundary layer mesh, its construction via an offset operation proves to be a particularly natural and intuitive choice. Three approaches for generating offset geometries that preserve the original parametric representation of the boundary layer were compared. Special cases may arise when the local radius of curvature is smaller than the offset thickness, which can lead to self-intersections; the treatment of such situations will be addressed in future work.

To couple the overlapping meshes, a standard mortar-type method was implemented. Numerical experiments demonstrated its usability, showing that the method remains stable when both meshes share identical material parameters, independently of the mesh size ratio. Several numerical examples further validated the proposed embedded mesh approach. In addition, the spatial convergence of the discretization were verified for contact problems. Finally, a three-dimensional large-deformation contact example was presented.

Overall, the proposed discretization approach constitutes an attractive framework for contact problems, as it combines the high continuity and smoothness of NURBS B-reps at contact interfaces with a straightforward and flexible mesh generation strategy for the bulk domain.

Future work will focus on coupling techniques that are fully insensitive to mesh locking, such as Nitsche’s method. Furthermore, ghost element stabilization techniques for configurations involving small cut-element volumes will be investigated. Finally, the capabilities of the proposed approach will be explored in the context of more complex three-dimensional geometries.

## Acknowledgements

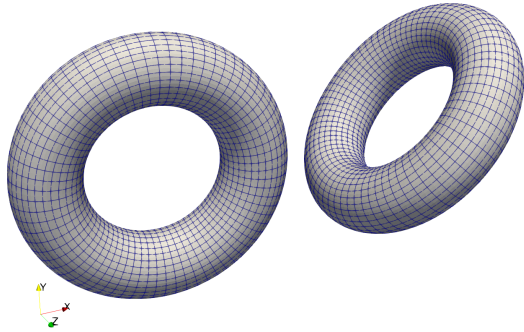
This work was supported by the Deutsche Forschungsgemeinschaft (DFG) - Project number 446494172.

## Declaration of generative AI and AI-assisted technologies in the manuscript preparation process.

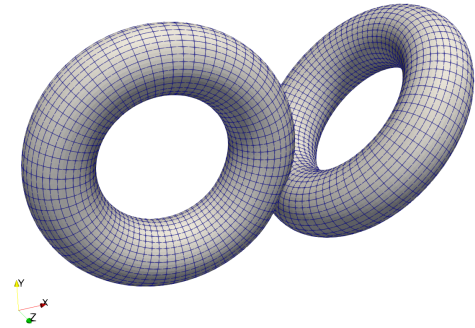
During the preparation of this work the author(s) used ChatGPT in order to improve the readability and language of the present script. After using this tool, the author(s) reviewed and edited the content as needed and take(s) full responsibility for the content of the published article.

## References

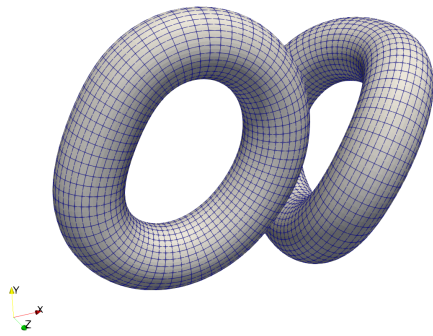
- [1] S. Dong and A. Sheldon, “Characterization and modeling of engineering friction and wear with LS-DYNA,” in *Proceedings of the 11th European LS-DYNA Conference*, (Salzburg, Austria), 2017.
- [2] U. Obaidallah, Z. Radzi, N. A. Yahya, N. A. Abu Osman, and A. F. Merican, “A finite element approach for the planning and simulation of 3D reconstruction of maxillofacial deformities,” in *4th Kuala Lumpur International Conference on Biomedical Engineering 2008* (N. A. Abu Osman, F. Ibrahim, W. A. B. Wan Abas, H. S. Abdul Rahman, and H.-N. Ting, eds.), (Berlin, Heidelberg), pp. 727–729, Springer Berlin Heidelberg, 2008.
- [3] M. Frank, F. Holzberger, M. Horvat, J. Kirschke, M. Mayr, M. Muhr, N. Nebulishvili, A. Popp, J. Schwarting, and B. Wohlmuth, “Numerical simulation of endovascular treatment options for cerebral aneurysms,” *GAMM-Mitteilungen*, vol. 47, no. 3, p. e202370007, 2024.
- [4] P. Wriggers, T. Vu Van, and E. Stein, “Finite element formulation of large deformation impact-contact problems with friction,” *Computers & Structures*, vol. 37, no. 3, pp. 319–331, 1990.



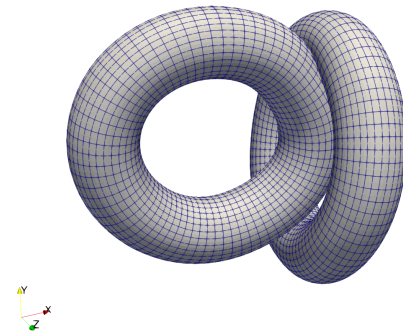
(a)  $t = 0.0$



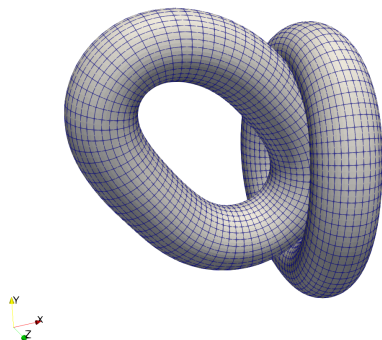
(b)  $t = 0.4$



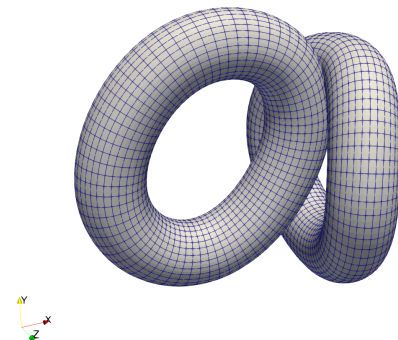
(c)  $t = 0.8$



(d)  $t = 1.2$



(e)  $t = 1.6$



(f)  $t = 2.0$

Figure 26: Two tori in contact - initial configuration and characteristic stages of deformation.

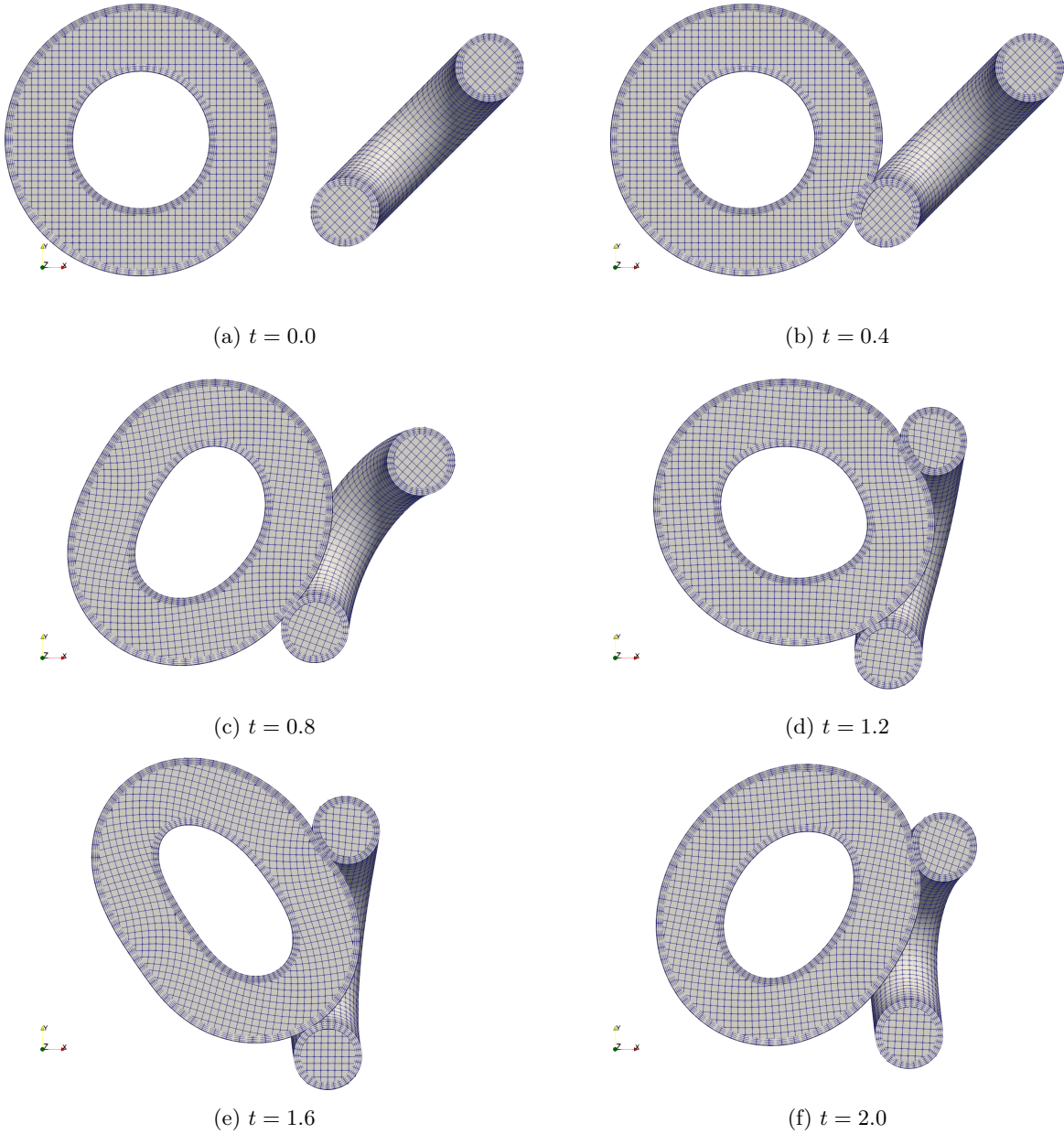


Figure 27: Two tori in contact in side view - initial configuration and characteristic stages of deformation.

- [5] P. Papadopoulos and R. L. Taylor, “A mixed formulation for the finite element solution of contact problems,” *Computer Methods in Applied Mechanics and Engineering*, vol. 94, no. 3, pp. 373–389, 1992.
- [6] G. Zavarise and L. De Lorenzis, “The node-to-segment algorithm for 2D frictionless contact: Classical formulation and special cases,” *Computer Methods in Applied Mechanics and Engineering*, vol. 198, no. 41, pp. 3428–3451, 2009.
- [7] G. Zavarise and P. Wriggers, “A segment-to-segment contact strategy,” *Mathematical and Computer Modelling*, vol. 28, no. 4, pp. 497–515, 1998.
- [8] K. A. Fischer and P. Wriggers, “Frictionless 2D contact formulations for finite deformations based on the mortar method,” *Computational Mechanics*, vol. 36, no. 3, pp. 226–244, 2005.
- [9] M. Puso and T. Laursen, “A mortar segment-to-segment contact method for large deformations,” *Computer Methods in Applied Mechanics and Engineering*, vol. 193, pp. 601–629, 02 2004.
- [10] F. Ben Belgacem, “Numerical simulation of some variational inequalities arisen from unilateral contact problems by the finite element methods,” *SIAM Journal on Numerical Analysis*, vol. 37, no. 4, pp. 1198–1216, 2000.
- [11] B. I. Wohlmuth and R. H. Krause, “Monotone multigrid methods on nonmatching grids for nonlinear multibody contact problems,” *SIAM Journal on Scientific Computing*, vol. 25, no. 1, pp. 324–347, 2003.
- [12] A. Popp, M. W. Gee, and W. A. Wall, “A finite deformation mortar contact formulation using a primal–dual active set strategy,” *International Journal for Numerical Methods in Engineering*, vol. 79, no. 11, pp. 1354–1391, 2009.
- [13] L. De Lorenzis, P. Wriggers, and C. Weißenfels, “Computational contact mechanics with the finite element method,” in *Encyclopedia of Computational Mechanics* (E. Stein, R. De Borst, and T. J. Hughes, eds.), pp. 1–45, Chichester, New York: Wiley, 2 ed., 2017.
- [14] B. I. Wohlmuth, A. Popp, M. W. Gee, and W. A. Wall, “An abstract framework for a priori estimates for contact problems in 3D with quadratic finite elements,” *Computational Mechanics*, vol. 49, pp. 735–747, 2012.
- [15] L. De Lorenzis, P. Wriggers, and T. J. Hughes, “Isogeometric contact: a review,” *GAMM-Mitteilungen*, vol. 37, no. 1, pp. 85–123, 2014.
- [16] I. Temizer, P. Wriggers, and T. Hughes, “Three-dimensional mortar-based frictional contact treatment in isogeometric analysis with NURBS,” *Computer Methods in Applied Mechanics and Engineering*, vol. 209–212, pp. 115–128, 2012.
- [17] V. Padmanabhan and T. Laursen, “A framework for development of surface smoothing procedures in large deformation frictional contact analysis,” *Finite Elements in Analysis and Design*, vol. 37, no. 3, pp. 173–198, 2001.
- [18] P. Wriggers, L. Krstulovic-Opara, and J. Korelc, “Smooth  $C^1$ -interpolations for two-dimensional frictional contact problems,” *International Journal for Numerical Methods in Engineering*, vol. 51, no. 12, pp. 1469–1495, 2001.
- [19] M. Al-Dojayli and S. Meguid, “Accurate modeling of contact using cubic splines,” *Finite Elements in Analysis and Design*, vol. 38, no. 4, pp. 337–352, 2002.
- [20] M. Tur, E. Giner, F. Fuenmayor, and P. Wriggers, “2D contact smooth formulation based on the mortar method,” *Computer Methods in Applied Mechanics and Engineering*, vol. 247–248, pp. 1–14, 2012.
- [21] D. M. Neto, M. C. Oliveira, and L. F. Menezes, “Surface smoothing procedures in computational contact mechanics,” *Archives of Computational Methods in Engineering*, vol. 24, no. 1, pp. 37–87, 2017.

- [22] T. Hughes, J. Cottrell, and Y. Bazilevs, “Isogeometric analysis: CAD, finite elements, NURBS, exact geometry and mesh refinement,” *Computer Methods in Applied Mechanics and Engineering*, vol. 194, no. 39, pp. 4135–4195, 2005.
- [23] J. A. Cottrell, T. J. Hughes, and Y. Bazilevs, *Isogeometric analysis: toward integration of CAD and FEA*. John Wiley & Sons, 2009.
- [24] J. A. Evans, Y. Bazilevs, I. Babuška, and T. J. Hughes, “n-Widths, sup-infs, and optimality ratios for the k-version of the isogeometric finite element method,” *Computer Methods in Applied Mechanics and Engineering*, vol. 198, no. 21, pp. 1726–1741, 2009.
- [25] D. Großmann, B. Jüttler, H. Schlusnus, J. Barner, and A.-V. Vuong, “Isogeometric simulation of turbine blades for aircraft engines,” *Computer Aided Geometric Design*, vol. 29, no. 7, pp. 519–531, 2012.
- [26] T. Kuraishi, K. Takizawa, and T. E. Tezduyar, “A general-purpose IGA mesh generation method: NURBS surface-to-volume guided mesh generation,” *Computational Mechanics*, 2024.
- [27] E. Wobbes, Y. Bazilevs, T. Kuraishi, Y. Otoguro, K. Takizawa, and T. E. Tezduyar, “Complex-geometry IGA mesh generation: application to structural vibrations,” *Computational Mechanics*, vol. 74, no. 2, pp. 247–261, 2024.
- [28] T. Martin, E. Cohen, and R. M. Kirby, “Volumetric parameterization and trivariate B-Spline fitting using harmonic functions,” *Comput. Aided Geom. Des.*, vol. 26, pp. 648–664, 2008.
- [29] H. A. Akhras, T. Elguedj, A. Gravouil, and M. Rochette, “Isogeometric analysis-suitable trivariate NURBS models from standard B-Rep models,” *Computer Methods in Applied Mechanics and Engineering*, vol. 307, pp. 256–274, 2016.
- [30] Y. Zheng and F. Chen, “Volumetric parameterization with truncated hierarchical B-Splines for isogeometric analysis,” *Computer Methods in Applied Mechanics and Engineering*, vol. 401, p. 115662, 2022.
- [31] E. Rank, M. Ruess, S. Kollmannsberger, D. Schillinger, and A. Düster, “Geometric modeling, isogeometric analysis and the finite cell method,” *Computer Methods in Applied Mechanics and Engineering*, vol. 249–252, pp. 104–115, 2012.
- [32] E. Burman, S. Claus, P. Hansbo, M. G. Larson, and A. Massing, “CutFEM: Discretizing geometry and partial differential equations,” *International Journal for Numerical Methods in Engineering*, vol. 104, no. 7, pp. 472–501, 2015.
- [33] H. Ji and J. E. Dolbow, “On strategies for enforcing interfacial constraints and evaluating jump conditions with the extended finite element method,” *International Journal for Numerical Methods in Engineering*, vol. 61, no. 14, pp. 2508–2535, 2004.
- [34] N. Moës, E. Béchet, and M. Tourbier, “Imposing Dirichlet boundary conditions in the extended finite element method,” *International Journal for Numerical Methods in Engineering*, vol. 67, no. 12, pp. 1641–1669, 2006.
- [35] M. A. Puso, J. Sanders, R. Settghost, and B. Liu, “An embedded mesh method in a multiple material ALE,” *Computer Methods in Applied Mechanics and Engineering*, vol. 245–246, pp. 273–289, 2012.
- [36] U. M. Mayer, A. Gerstenberger, and W. A. Wall, “Interface handling for three-dimensional higher-order XFEM-computations in fluid–structure interaction,” *International Journal for Numerical Methods in Engineering*, vol. 79, no. 7, pp. 846–869, 2009.
- [37] B. Schott, S. Shahmiri, R. Kruse, and W. Wall, “A stabilized Nitsche-type extended embedding mesh approach for 3D low- and high-Reynolds-number flows,” *International Journal for Numerical Methods in Fluids*, vol. 82, no. 6, pp. 289–315, 2016.
- [38] N. Moës, J. Dolbow, and T. Belytschko, “A finite element method for crack growth without remeshing,” *International Journal for Numerical Methods in Engineering*, vol. 46, no. 1, pp. 131–150, 1999.

- [39] A. B. Groeneveld and P. Chen, “An immersed finite element method for interfacial damage and debonding,” *Computational Mechanics*, vol. 75, no. 5, pp. 1555–1583, 2025.
- [40] X. Wei, B. Marussig, P. Antolin, and A. Buffa, “Immersed boundary-conformal isogeometric method for linear elliptic problems,” *Comput. Mech.*, vol. 68, p. 1385–1405, Dec. 2021.
- [41] G. Guarino, A. Milazzo, A. Buffa, and P. Antolin, “The immersed boundary conformal method for Kirchhoff–Love and Reissner–Mindlin shells,” *Computer Methods in Applied Mechanics and Engineering*, vol. 432, p. 117407, 2024.
- [42] J. D. Sanders, T. A. Laursen, and M. A. Puso, “A Nitsche embedded mesh method,” *Computational Mechanics*, vol. 49, no. 2, pp. 243–257, 2012.
- [43] É. Béchet, N. Moës, and B. Wohlmuth, “A stable Lagrange multiplier space for stiff interface conditions within the extended finite element method,” *International Journal for Numerical Methods in Engineering*, vol. 78, no. 8, pp. 931–954, 2009.
- [44] I. Nistor, M. Guiton, P. Massin, N. Moes, and S. Géniaut, “An X-FEM approach for large sliding contact along discontinuities,” *International Journal for Numerical Methods in Engineering*, vol. 78, no. 12, pp. 1407–1435, 2009.
- [45] D. S. Malkus and T. J. Hughes, “Mixed finite element methods — reduced and selective integration techniques: A unification of concepts,” *Computer Methods in Applied Mechanics and Engineering*, vol. 15, no. 1, pp. 63–81, 1978.
- [46] J. C. Simo and F. Armero, “Geometrically non-linear enhanced strain mixed methods and the method of incompatible modes,” *International Journal for Numerical Methods in Engineering*, vol. 33, no. 7, pp. 1413–1449, 1992.
- [47] W. T. Les Piegl, *The NURBS Book*. Springer Berlin, Heidelberg, 1995.
- [48] M. G. Cox, “The numerical evaluation of B-Splines,” *IMA Journal of Applied Mathematics*, vol. 10, pp. 134–149, 10 1972.
- [49] C. de Boor, “On calculating with B-Splines,” *Journal of Approximation Theory*, vol. 6, no. 1, pp. 50–62, 1972.
- [50] S.-H. Chuang and J.-L. Shih, “A novel approach for computing  $C^2$ -continuous offset of NURBS curves,” *The International Journal of Advanced Manufacturing Technology*, vol. 29, pp. 151–158, 2006.
- [51] G. Elber, I.-K. Lee, and M.-S. Kim, “Comparing offset curve approximation methods,” *IEEE Computer Graphics and Applications*, vol. 17, no. 3, pp. 62–71, 1997.
- [52] J.-L. Shih and S.-H. Frank Chuang, “One-sided offset approximation of freeform curves for interference-free NURBS machining,” *Computer-Aided Design*, vol. 40, no. 9, pp. 931–937, 2008.
- [53] W. Tiller and E. G. Hanson, “Offsets of two-dimensional profiles,” *IEEE Computer Graphics and Applications*, vol. 4, no. 9, pp. 36–46, 1984.
- [54] L. A. Piegl and W. Tiller, “Computing offsets of NURBS curves and surfaces,” *Computer-Aided Design*, vol. 31, no. 2, pp. 147–156, 1999.
- [55] T. Greville, “Introduction to Spline functions,” *Theory and applications of Spline functions*, vol. 22, pp. 1–36, 1969.
- [56] V. P. Nguyen, P. Kerfriden, S. P. A. Bordas, and T. Rabczuk, “Isogeometric analysis suitable trivariate NURBS representation of composite panels with a new offset algorithm,” *Comput. Aided Des.*, vol. 55, p. 49–63, oct 2014.
- [57] P. Farah, W. A. Wall, and A. Popp, “A mortar finite element approach for point, line, and surface contact,” *International Journal for Numerical Methods in Engineering*, vol. 114, no. 3, pp. 255–291, 2018.
- [58] D. W. Yavuz Başar, *Nonlinear Continuum Mechanics of Solids*. Springer Berlin, Heidelberg, 2000.

- [59] P. Wriggers, *Computational contact mechanics*. Springer-Verlag Berlin Heidelberg, 2006.
- [60] S. C. Brenner and C. Carstensen, “Finite element methods,” in *Encyclopedia of Computational Mechanics Second Edition*, pp. 1–47, John Wiley & Sons, Ltd, 2017.
- [61] B. I. Wohlmuth, “A Mortar Finite Element Method Using Dual Spaces for the Lagrange Multiplier,” *SIAM Journal on Numerical Analysis*, vol. 38, no. 3, pp. 989–1012, 2000.
- [62] S. Hübner and B. Wohlmuth, “A primal–dual active set strategy for non-linear multibody contact problems,” *Computer Methods in Applied Mechanics and Engineering*, vol. 194, no. 27, pp. 3147–3166, 2005.
- [63] A. Popp, B. I. Wohlmuth, M. W. Gee, and W. A. Wall, “Dual Quadratic Mortar Finite Element Methods for 3D Finite Deformation Contact,” *SIAM Journal on Scientific Computing*, vol. 34, no. 4, pp. B421–B446, 2012.
- [64] S. Hartmann, S. Brunssen, E. Ramm, and B. Wohlmuth, “Unilateral non-linear dynamic contact of thin-walled structures using a primal-dual active set strategy,” *International Journal for Numerical Methods in Engineering*, vol. 70, no. 8, pp. 883–912, 2007.
- [65] A. Popp, M. Gitterle, M. W. Gee, and W. A. Wall, “A dual mortar approach for 3D finite deformation contact with consistent linearization,” *International Journal for Numerical Methods in Engineering*, vol. 83, no. 11, pp. 1428–1465, 2010.
- [66] A. Seitz, P. Farah, J. Kremheller, B. I. Wohlmuth, W. A. Wall, and A. Popp, “Isogeometric dual mortar methods for computational contact mechanics,” *Computer Methods in Applied Mechanics and Engineering*, vol. 301, pp. 259–280, 2016.
- [67] L. R. Scott, , and S. Zhang, “Finite element interpolation of nonsmooth functions satisfying boundary conditions,” *Mathematics of Computation*, vol. 54, pp. 483–493, 1990.
- [68] S. Hübner, *Discretization techniques and efficient algorithms for contact problems*. PhD thesis, 01 2008.
- [69] A. J. Lew and G. C. Buscaglia, “A discontinuous-Galerkin-based immersed boundary method,” *International Journal for Numerical Methods in Engineering*, vol. 76, no. 4, pp. 427–454, 2008.
- [70] J. Nitsche, “Über ein Variationsprinzip zur lösung von Dirichlet-Problemen bei Verwendung von Teilräumen, die keinen Randbedingungen unterworfen sind,” *Abhandlungen aus dem Mathematischen Seminar der Universität Hamburg*, vol. 36, no. 1, pp. 9–15, 1971.
- [71] J. Sanders and M. A. Puso, “An embedded mesh method for treating overlapping finite element meshes,” *International Journal for Numerical Methods in Engineering*, vol. 91, no. 3, pp. 289–305, 2012.
- [72] M. Hintermüller, K. Ito, and K. Kunisch, “The primal-dual active set strategy as a semismooth newton method,” *SIAM Journal on Optimization*, vol. 13, no. 3, pp. 865–888, 2002.
- [73] M. Gitterle, A. Popp, M. W. Gee, and W. A. Wall, “Finite deformation frictional mortar contact using a semi-smooth newton method with consistent linearization,” *International Journal for Numerical Methods in Engineering*, vol. 84, no. 5, pp. 543–571, 2010.
- [74] B. Yang, T. A. Laursen, and X. Meng, “Two dimensional mortar contact methods for large deformation frictional sliding,” *International Journal for Numerical Methods in Engineering*, vol. 62, pp. 1183–1225, Dec 2004.
- [75] I. Steinbrecher, M. Mayr, M. J. Grill, J. Kremheller, C. Meier, and A. Popp, “A mortar-type finite element approach for embedding 1D beams into 3D solid volumes,” *Computational Mechanics*, vol. 66, pp. 1377–1398, Dec 2020.
- [76] I. Steinbrecher, A. Popp, and C. Meier, “Consistent coupling of positions and rotations for embedding 1D Cosserat beams into 3D solid volumes,” *Computational Mechanics*, vol. 69, no. 3, pp. 701–732, 2022.

- [77] I. Steinbrecher, N. Hagemeyer, C. Meier, and A. Popp, “A consistent mixed-dimensional coupling approach for 1D Cosserat beams and 2D surfaces in 3D space,” *Computational Mechanics*, vol. 76, no. 5, pp. 1233–1260, 2025.
- [78] M. A. Puso, T. Laursen, and J. Solberg, “A segment-to-segment mortar contact method for quadratic elements and large deformations,” *Computer Methods in Applied Mechanics and Engineering*, vol. 197, no. 6, pp. 555–566, 2008.
- [79] C. Hesch and P. Betsch, “Isogeometric analysis and domain decomposition methods,” *Computer Methods in Applied Mechanics and Engineering*, vol. 213–216, pp. 104–112, 2012.
- [80] M. Dittmann, M. Franke, I. Temizer, and C. Hesch, “Isogeometric analysis and thermomechanical mortar contact problems,” *Computer Methods in Applied Mechanics and Engineering*, vol. 274, pp. 192–212, 2014.
- [81] U. M. Mayer, A. Popp, A. Gerstenberger, and W. A. Wall, “3D fluid-structure-contact interaction based on a combined XFEM FSI and dual mortar contact approach,” *Computational Mechanics*, vol. 46, no. 1, pp. 53–67, 2010.
- [82] M. Winter, B. Schott, A. Massing, and W. Wall, “A Nitsche cut finite element method for the Oseen problem with general Navier boundary conditions,” *Computer Methods in Applied Mechanics and Engineering*, vol. 330, pp. 220–252, 2018.
- [83] Y. Sudhakar, J. Moitinho de Almeida, and W. A. Wall, “An accurate, robust, and easy-to-implement method for integration over arbitrary polyhedra: Application to embedded interface methods,” *Journal of Computational Physics*, vol. 273, pp. 393–415, 2014.
- [84] O. R. Bingol and A. Krishnamurthy, “NURBS-Python: An open-source object-oriented NURBS modeling framework in Python,” *SoftwareX*, vol. 9, pp. 85–94, 2019.
- [85] BeamMe Authors, “BeamMe – A general purpose 3D beam finite element input generator.” <https://beamme-py.github.io/beamme>, 2026. Accessed: February 20th.
- [86] 4C, “4C: A Comprehensive Multiphysics Simulation Framework.” <https://www.4c-multiphysics.org>, 2026. Accessed: February 20th.
- [87] B. M. Irons and A. Razzaque, “Experience with the patch test for convergence of finite elements,” in *The Mathematical Foundations of the Finite Element Method with Applications to Partial Differential Equations* (A. Aziz, ed.), pp. 557–587, Academic Press, 1972.
- [88] N. El-Abbasi and K.-J. Bathe, “Stability and patch test performance of contact discretizations and a new solution algorithm,” *Computers & Structures*, vol. 79, no. 16, pp. 1473–1486, 2001.
- [89] A. Popp, A. Seitz, M. W. Gee, and W. A. Wall, “Improved robustness and consistency of 3D contact algorithms based on a dual mortar approach,” *Computer Methods in Applied Mechanics and Engineering*, vol. 264, pp. 67–80, 2013.
- [90] N. Kikuchi and J. T. Oden, *Contact Problems in Elasticity*. Society for Industrial and Applied Mathematics, 1988.
- [91] B. Yang and T. A. Laursen, “A contact searching algorithm including bounding volume trees applied to finite sliding mortar formulations,” *Computational Mechanics*, vol. 41, no. 2, pp. 189–205, 2008.